RIM and RIM-binding protein localize synaptic Ca_v2 channels in a differential manner to regulate transmission in neuronal circuits

Barbara Jánosi[1,2,3], Jana F. Liewald[1,2,3], Szi-chieh Yu[1,2,4], Simon Umbach[1,2], Ivan C. Alcantara[1,2,5], Amelie C.F. Bergs[1,2], Martin Schneider[1,2,6], Jiajie Shao[1,2], Alexander Gottschalk[1,2,*]

1 Buchmann Institute for Molecular Life Sciences, Goethe-University, Max-von-Laue-Strasse 15, D-60438 Frankfurt, Germany
2 Department of Biochemistry, Chemistry and Pharmacy, Institute for Biophysical Chemistry, Goethe-University, Max-von-Laue-Strasse 9, D-60438 Frankfurt, Germany
3 these authors contributed equally
4 current address: Princeton Neuroscience Institute, Princeton University, Princeton, NJ 08544, USA
5 current address: National Institute of Diabetes and Digestive and Kidney Disease, National Institutes of Health, Bethesda, MD 20814, USA
6 current address: Max-Planck-Institute for Neurobiologie, Department of Genes – Circuits – Behavior, Am Klopferspitz 18, D-82152 Martinsried, Germany

*Correspondence and lead contact: a.gottschalk@em.uni-frankfurt.de

Short title: RIM and RIMB-1 jointly localize the Ca_v2 VGCC to docked synaptic vesicles

Abstract

Synapses are intricately organized subcellular compartments in which molecular machines cooperate to ensure spatiotemporally precise transmission of chemical signals. Key components of this machinery are voltage-gated Ca^{2+}-channels (VGCCs), that translate electrical signals into a trigger for fusion of synaptic vesicles (SVs) with the plasma membrane. The VGCCs and the Ca^{2+} microdomains they generate must be located in the right distance to the primed SV, to elicit transmitter release without delay. Rab3 interacting molecule (RIM) and RIM-binding protein (RIM-BP) were shown in different systems to contribute to the spatial organization of the active zone protein scaffold, and to localize VGCCs next to docked SVs by binding to each other and to the C-terminal region of the Ca_v2 VGCC α-subunit. We asked how this machinery is organized at the neuromuscular junction (NMJ) of *Caenorhabditis elegans*, and whether it can differentially regulate transmission in circuits composed of different neuron types. *rimb-1* mutants had mild synaptic defects, through loosening the anchoring of the UNC-2 VGCC and delaying the onset of SV fusion, while RIM deletion had much more severe defects. *rimb-1* mutants caused increased cholinergic but reduced GABAergic transmission, while overall transmission at the NMJ was reduced, as shown by voltage imaging. The UNC-2 channel could further be untethered by removing its C-terminal PDZ binding motif, and this untethering could be exacerbated by combining the ΔPDZ mutant with the *rimb-1* mutation. Similar phenotypes resulted from acute degradation of the UNC-2 β-subunit, indicating that destabilization of the VGCC complex causes the same phenotypes as its untethering.

Keywords: synaptic vesicle cycle, active zone, RIMB-1, RBP, RIM, voltage gated Ca^{2+} channels, VGCC, *Caenorhabditis elegans*

Introduction

Neurons transmit chemical signals from synaptic terminals, by release from synaptic vesicles (SVs) that fuse with the plasma membrane (Brunger et al., 2018; Sudhof, 2013). This process is triggered by action potentials arriving at the terminal, and activation of voltage gated Ca^{2+} channels (VGCCs) that mediate a rapid, local rise in the concentration of cytosolic Ca^{2+} (Nanou and Catterall, 2018). This signal is detected by the Ca^{2+} sensor for synchronous release, synaptotagmin, which is an intrinsic component of SVs (Sudhof, 2012). Protein complexes intricately organize SVs and P/Q-type VGCCs ($Ca_v2.1$ in mammals, UNC-2 in *Caenorhabditis elegans*) in the presynaptic active zone membrane, to ensure an optimal distance for rapid Ca^{2+} sensing (Acuna et al., 2015; Acuna et al., 2016; Han et al., 2011; Held et al., 2020; Hibino et al., 2002; Kaeser et al., 2011; Liu et al., 2011; Wu et al., 2019). While SNARE complexes hold the SV in a configuration ready to catalyze membrane fusion upon the Ca^{2+} signal, the VGCC is held in place by a complex of the RIM protein (RAB3 interacting molecule) and the RIM-binding protein (RIMBP), via its C-terminal tail. RIM binds to the SV via RAB3 proteins, and to other components of the active zone protein scaffold, termed presynaptic particle web in mammals, cytomatrix of the active zone (CAZ) in *Drosophila*, or dense projection in *C. elegans* (Ackermann et al., 2015).

In recent years the function of RIMBPs (RIMB-1 in *C. elegans*) was elucidated in mammalian and *Drosophila* neurons (Acuna et al., 2015; Acuna et al., 2016; Brockmann et al., 2019; Brockmann et al., 2020; Liu et al., 2011; Muller et al., 2015). While mice lacking both neuronal RIM-BPs showed no alteration in synapse number and evoked release per se, the fidelity and timing of release in response to evoked action potentials was decreased (Acuna et al., 2015). In calyx of held synapses, also the evoked post-synaptic current (ePSC) amplitude was decreased in RIM-BP1,2 double knockout mice. RIM-BPs were shown to anchor Ca_v2 in vicinity to primed SVs, by binding the VGCC C-terminus, however, they did not affect VGCC function or kinetics. The fly mutant *drbp* showed a more severe phenotype, with reduced Ca^{2+} sensitivity of release, and a defect in presynaptic homeostatic plasticity (Liu et al., 2011; Muller et al., 2015). This was because neurons could not potentiate Ca^{2+} influx, an otherwise normal response to the blocking of post-synaptic transmitter receptors, which involves coupling of VGCCs to docked SVs. In *Drosophila*, *drbp* was genetically interacting with *rim* during baseline transmission, with similar phenotypes of both mutants, and more severe phenotypes if they were combined. RIM-BP was also affecting SV recycling after extensive synaptic activity (Muller et al., 2015). The interaction of RIM and RIM-BPs in mice is also present, however, here RIM has a more central function in recruiting and stabilizing VGCCs at synapses. Yet, in mammals, RIM deletion alone does not affect synaptic function as severely as in *C. elegans* (Koushika et al., 2001), and interestingly, RIM and RIM-BPs exhibit redundant function in mice, affecting synaptic transmission through the absence of active zone VGCCs, but also the assembly of the active zone protein scaffold, and recruitment of Munc13 proteins, which are essential for SV priming (Acuna et al., 2016; Brockmann et al., 2019; Brockmann et al., 2020). This function may be achieved by RIM and RIM-BP forming a phase-separated condensate that functions in the dynamic organization of the active zone protein scaffold (Wu et al., 2019). In *C. elegans*, a transgenically overexpressed GFP::UNC-2 (Ca_v2) protein was enhanced in its expression by overexpressing RIMB-1, and in the *rimb-1*; *unc-10* (RIM) double mutants, as in mice, Ca_v2/UNC-2 channels were reduced in their synaptic abundance (Kushibiki et al., 2019). Vice versa, RIMB-1 was partly dependent on UNC-2 for its precise localization at the presynaptic active zone. The synaptic ultrastructure of the *C. elegans rimb-1* mutant was not yet

analyzed, and likewise it is not clear how absence of RIMB-1 and the likely consequent untethering of UNC-2/Ca_v2 channels affects synaptic properties and the characteristics of chemical transmission in *C. elegans*.

RIMB-1, the single *C. elegans* homolog of vertebrate RIM-BPs, contains three *src*-homology type III (SH3) domains, and three fibronectin type III (FN3) domains (**Fig. 1A**). RIM-BPs bind to proline-rich sequences of RIM (UNC-10) and the Ca_v2 $\alpha1$ subunit (UNC-2) via its SH3 domains (Hibino et al., 2002; Wu et al., 2019). UNC-10/RIM binds to the C-terminal end of Ca_v2/UNC-2 via its PSD95/Discs large/Zonula occludens (PDZ) domain (Kaeser et al., 2011), forming a tripartite complex (**Fig. 1B**). The interplay of these interactions in locating the Ca_v2 channel relative to the docked SV is not known in *C. elegans*. For example, does UNC-2 require both interactions for tight positioning, or is one of them (via RIM or via RIMB-1) sufficient to ensure fidelity in synaptic transmission? The neuromuscular junction (NMJ) of *C. elegans* is thought to be driven by graded, not action, potentials (Liu et al., 2009; Schultheis et al., 2011). Recent voltage imaging data suggest that cholinergic neurons may also produce fast, action-potential like activities (Azimi Hashemi et al., 2019), which may result from burst activity of the premotor interneurons that are presynaptic to cholinergic motor neurons (Liu et al., 2017). Thus, is faithful transmission at the millisecond time scale at all required in this synapse, or are the interactions between UNC-2, RIMB-1, and UNC-10/RIM merely required to anchor UNC-2 in the *en passant* synaptic terminals and to prevent them from lateral diffusion into the axon? The *C. elegans* NMJ is a tripartite synapse comprising cholinergic motor neurons that innervate muscle cells as well as GABAergic motor neurons, the latter of which projecting to the respective dorsal or ventral side of the body to innervate opposing muscle. This circuitry orchestrates the dorso-ventral undulatory locomotion, and muscles thus integrate activity of both cholinergic and GABAergic inputs. Precise function of synapses in both types of neurons is required to ensure normal excitation-inhibition balance, and this may involve anchoring of VGCCs. Previous work showed differential requirement of L- and P/Q-type VGCCs at cholinergic and GABAergic synapses in *C. elegans* (Liu et al., 2018).

Here, we set out to characterize in detail the synaptic phenotypes of *rimb-1* mutants at the behavioral, physiological, and ultrastructural level, and to address molecular details of its interaction with UNC-2/Ca_v2 channels. We find that RIMB-1 interacts with RIM in localizing the Ca_v2 channel UNC-2 and that incremental de-anchoring of the UNC-2 channel causes phenotypes that resemble its deletion. Furthermore, RIMB-1 differentially affects UNC-2 channels in different cell types, thus regulating the outcome of circuit function at different levels.

Results

RIMB-1 is expressed in cholinergic and GABAergic motor neurons

To verify the expression of *rimb-1* in neurons, specifically at the NMJ, we co-expressed GFP (*rimb-1* promoter, 3 kb upstream of the ATG) and mCherry (from the cholinergic neuron specific *unc-17* promoter; **Fig. 1C**). *rimb-1p*::GFP expressed throughout the nervous system, including motor neurons in the ventral nerve cord, while *unc-17p*::mCherry was observed in a subset of neurons, in which it overlapped with *rimb-1p*::GFP. Thus, *rimb-1* is likely pan-neuronal, and at the NMJ, it is expressed in both cholinergic and GABAergic motor neurons.

rimb-1 mutants exhibit reduced cholinergic transmission

We assessed possible defects in synaptic transmission of *rimb-1* animals. *rimb-1(tm5964)* mutants have a 659 bp deletion affecting exon 14 and the preceding intron, which likely leads to skipping of this exon, and a protein that misses 81 amino acids (positions 794-875) in-frame, in the second SH3 domain (**Fig. 1A**). Whether this represents a null allele is not known. In any case, this allele should affect the interaction of RIMB-1 and UNC-10/RIM, since it is mediated by this SH3 domain (Wang et al., 2000). First we assayed cholinergic transmission: Incubation in the acetylcholinesterase inhibitor aldicarb leads to progressive paralysis due to accumulation of acetylcholine (ACh) in the synaptic cleft and muscle hyper-contraction (Mahoney et al., 2006). We compared *rimb-1(tm5964)* mutants to *unc-10(md1117)* animals, as well as *rimb-1; unc-10* double mutants, and wild type controls (**Fig. 2A**). *rimb-1* animals paralyzed significantly later than controls, indicating defective ACh release. *unc-10* mutants, as well as *rimb-1; unc-10* animals, were much more compromised, not paralyzing during the time course of the assay, thus emphasizing a very strong reduction of synaptic transmission. Function of post-synaptic nicotinic acetylcholine receptors (nAChRs) was assessed by a similar paralysis assay using an agonist of the main *C. elegans* muscle nAChR: *rimb-1* mutants paralyzed as wild type, in contrast to the nAChR subunit mutant *unc-38* (**Fig. S1A**). Thus, post-synaptic nAChRs are normal in *rimb-1* animals.

Second, swimming behavior (**Fig. 2B**) was compromised in *rimb-1* mutants, which showed a significant reduction of the swimming rate, while *unc-10* as well as *rimb-1; unc-10* double mutants were much more affected, i.e. almost paralyzed. Here, *rimb-1* exacerbated the *unc-10* single mutant phenotype.

Third, we assessed cholinergic function by optogenetics. We expressed channelrhodopsin-2 (ChR2) in cholinergic neurons (transgene *zxIs6*) and photostimulated them for 60 s, which causes ACh release, muscle activation, and macroscopic body contraction (Liewald et al., 2008). Body length was measured before, during, and after photostimulation (**Fig. 2C, D**). Wild type animals contracted by about 10 %, *rimb-1* mutants only about 6 %. *rimb-1; unc-10* double mutants initially shrank like wild type, but showed a significant, progressive reduction in the contraction to about 6 %. This is indicative of synaptic fatigue, possibly due to a SV recycling defect (Kittelmann et al., 2013b). *rimb-1* mutants did not behave like typical SV release mutants (like synaptobrevin *snb-1*; **Fig. S1B, C**), because such mutants typically show increased contraction, due to a compensatory increase in post-synaptic excitability (Liewald et al., 2008). To explore this, we directly excited muscle via ChR2 in pre-synaptic release mutants (**Fig. S1D**): While *snb-1* mutants contracted more than controls, *rimb-1* animals behaved like wild type. In sum, *rimb-1* mutants showed complex synaptic transmission defects that could affect not only SV release, but also recycling, possibly through VGCC signaling. As RIMB-1 is expressed in cholinergic and GABAergic motor neurons, it likely affects NMJ transmission through both cell types.

rimb-1 mutants show delayed, but unexpectedly increased cholinergic ePSCs

To more directly assess transmission in *rimb-1(tm5964)*, *unc-10(md1117)*, and *rimb-1; unc-10* double mutants, we recorded post-synaptic currents in patch-clamped muscle cells. We analyzed spontaneous as well as evoked release, before and after repeated optogenetic

stimulation (*via zxIs6*; **Fig. 3A**). Muscles are also innervated by GABAergic neurons, thus we stimulated these in another set of experiments (transgene *zxIs3*, expression of ChR2 from *unc-47p*; **Fig. 3B**; note GABA induced currents appear as inward under the conditions used, i.e. -60 mV holding potential, and specific pipette and bath solutions, as described in materials and methods). *unc-10* and *rimb-1; unc-10* animals showed significantly reduced miniature post-synaptic current (mPSC) frequencies, while mPSC amplitudes were unaltered in all genetic backgrounds (**Fig. 3C, D**). Photostimulation evoked significantly increased PSC (ePSC) amplitudes in *rimb-1* mutants (**Fig. 3E, F**), that remained larger than in wild type for all repeated stimuli (0.5 Hz), while *unc-10* and *rimb-1; unc-10* animals showed significantly reduced ePSC amplitudes. The ePSC amplitude increase in *rimb-1* mutants was unexpected: If RIMB-1, as in mammals, mediated tight local arrangement of Ca_V2/UNC-2 and SVs, transmission should be reduced. We thus analyzed the parameters of evoked release in more detail (**Fig. 3G-I; S2-S4**), paying attention to the peak amplitude, delay from light pulse onset to peak current (time to peak), rise and decay times, and area under the curve (**Fig. 3G**). *rimb-1* mutants were delayed in their time to peak, particularly if combined with the *unc-10* RIM mutant, yet they exhibited a faster rise time (**Fig. 3I**). As for other organisms in which RIM-BPs were analyzed, this delay is in line with an effect removing P/Q-type VGCCs from primed SVs, such that they experience a delayed rise in Ca^{2+} concentration. These phenotypes were similar for the consecutive stimulations, though sometimes less pronounced, possibly because Ca^{2+} levels in the terminal remained elevated after the first stimulus (**Fig. S2C, S3, S4A, B**). Quantal content, calculated by dividing the area under the ePSC curve by the mean area under the mPSC peak (**Fig. 3J; S2A-C, S3B**), was differently distributed across measurements in wild type vs. *rimb-1* or *unc-10* mutants, and was significantly smaller in the *rimb-1; unc-10* mutants. Both proteins thus contribute to effective synaptic transmission at the *C. elegans* NMJ, possibly through jointly anchoring the UNC-2 channel to SV release sites.

GABAergic ePSCs and summed NMJ transmission are reduced in *rimb-1* mutants

Next, we analyzed GABAergic synapses to address if *rimb-1* was similarly required for GABAergic transmission. Over all time points, ePSCs were significantly smaller in *rimb-1; zxIs3* animals in which GABA neurons were specifically stimulated (**Fig. 3K, L**), while at the behavioral level, no difference was observed to wild type (**Fig. S5A, B**); normalized GABA ePSCs did not reveal any difference over time (**Fig. S5C**). The time to peak (GABA) was significantly delayed in *rimb-1* animals (**Fig. 3M**), while quantal content was unaltered (**Fig. 3N**). Thus, mutation of *rimb-1* delayed transmission in both cholinergic and GABAergic synapses, while it increased (ACh) or reduced (GABA) peak ePSCs.

The somewhat contradictory outcome of the optogenetically evoked PSC experiments in the two cell types may be affected by the synaptic organization of the *C. elegans* NMJ (**Fig. 4A, B**): During locomotion, ventral cholinergic activity evokes concomitant dorsal GABAergic inhibition of muscle (and vice versa), thus optogenetic stimulation of cholinergic transmission also evokes GABA transmission. To more clearly assess this, we recorded spontaneous and cholinergic neuron (*zxIs6*) evoked PSCs at a different holding potential, where GABA induced currents appear as outward (**Fig. S6A**). We observed a trend to reduced mPSC frequency for both ACh and GABA, and unaltered amplitudes (**Fig. S6B, C**). Evoked PSCs were delayed, and smaller in *rimb-1* mutants, likely due to a difference in summed (simultaneously evoked) ACh and GABA currents (**Fig. S6D-H**).

The summed effect of cholinergic and GABAergic signaling at the NMJ is difficult to measure by electrophysiology, as it depends on intact commissural connections from ventral to dorsal that may be severed during the dissection. Thus, we also employed *in vivo* muscle voltage imaging in intact animals (**Fig. 4C**). The archaerhodopsin variant D95N shows membrane voltage dependent fluorescence (Azimi Hashemi et al., 2019; Hochbaum et al., 2014; Kralj et al., 2012; **Fig. 4B**). Imaging Arch(D95N) fluorescence (730 nm) before, during, and after 10 s photostimulation of cholinergic neurons, demonstrated largely reduced muscle depolarization in *rimb-1* mutants (**Fig. 4C**), in line with the behavioral defects of *rimb-1* animals.

Our findings suggest that upon cholinergic stimulation, *rimb-1* mutants release ACh and GABA, at reduced levels. Depending on recording conditions (holding potential), the summed evoked currents appear increased or reduced. GABA release is more affected by *rimb-1*, and by integrating both types of transmission, muscles become less depolarized and locomotion is defective in these mutants.

***rimb-1* defects are more pronounced in the absence of GABA transmission**

To further probe the role of *rimb-1* in GABA transmission at the NMJ, we stimulated cholinergic neurons in *unc-47(e307)* mutants lacking the vesicular GABA transporter (vGAT), and in *unc-47; rimb-1* double mutants. vGAT mutants contracted much more than wild type, since all inhibitory transmission is abolished (**Fig. 4D**). In *rimb-1; unc-47* double mutants, the contractions were similar to wild type, i.e. in-between the single mutants. In addition, the double mutants showed a significant, progressive fatigue (i.e. SV recycling phenotype), as observed for *rimb-1* single mutants, though more pronounced. Thus, the lack of GABA transmission emphasizes the role of RIMB-1 in cholinergic transmission and SV recycling. mPSC frequency was significantly reduced in *unc-47* and (by about 80%) in *rimb-1; unc-47* double mutants (**Fig. 4E**), and likewise, mPSC amplitudes were significantly reduced in *rimb-1; unc-47* double mutants (**Fig. 4F**). A different trend was seen again for photoevoked PSCs: Amplitudes were not significantly different in this set of experiments, though *rimb-1* mutants showed again a tendency to higher amplitude, while this was abolished in the *rimb-1; unc-47* double mutant (**Fig. 4G**), indicating that the increased ePSC amplitude is predominantly caused (or compensated) by GABAergic neurons. This was also indicated by repeated photostimulation: *rimb-1; unc-47* double mutants showed the strongest fatigue and smaller consecutive ePSCs (**Fig. 4H; S5D**). RIMB-1 may affect GABAergic neurons in a similar way as cholinergic neurons, though due to the larger size of GABA neuron terminals (Kittelmann et al., 2013a), precise localization of UNC-2 VGCCs to the vicinity of SV docking sites may be more important in these neurons.

RIMB-1 affects the location of SV fusion sites in the active zone

RIMB-1, together with UNC-10/RIM, aligns UNC-2 VGCCs with primed SVs, ensuring that upon depolarization, Ca^{2+} microdomains are generated most effectively. Thus, the site of SV fusion, but possibly also the overall arrangement of the active zone (AZ), may be affected by the loss of RIMB-1 function. The *C. elegans* AZ plasma membrane harbors the dense projection (DP) at its center. We analyzed the ultrastructure of wild type and *rimb-1* mutant synapses by serial section transmission electron microscopy (TEM) (Kittelmann et al., 2013b). 40 nm thin sections of high-pressure frozen (HPF), freeze-substituted and stained samples were analyzed, in resting or photostimulated animals (*zxIs6*) (Kittelmann et al., 2013b; Steuer Costa et al., 2017; Yu et al., 2018). Following 30 s illumination, in animals grown in presence or absence of all-*trans* retinal (ATR; thus rendering ChR2 active or

inactive), total SVs, docked SVs, dense core vesicles (DCVs), and SV-recycling induced large vesicles (LVs) were quantified (**Fig. 5A**). Total SVs were slightly, but significantly reduced in *rimb-1* synapses, and photostimulation led to a more pronounced decrease in SV numbers in *rimb-1* mutants compared to wild type (**Fig. 5B**). This is surprising, since given the reduced fidelity of transmission in *rimb-1* mutants, one would expect reduced release and higher numbers of (docked) SVs. Possibly RIMB-1 is also required for SV docking. Indeed, there were significantly less docked SVs in *rimb-1* synapses, before and after photostimulation (**Fig. 5C**). DCV numbers were not affected by *rimb-1* or photostimulation (**Fig. 5C**; note DCV release in cholinergic neurons requires an increase in cAMP; Steuer Costa et al., 2017). Large vesicles, i.e. endosomes induced by photostimulation, were significantly increased in wild type photostimulated animals, but not in *rimb-1* synapses (**Fig. 5E**), in line with the reduced overall synaptic activity observed in our other experiments. DP size was not significantly different in wild type vs. *rimb-1* mutants, as in mammalian synapses (Acuna et al., 2016; **Fig. S7A**).

Next, we analyzed the occurrence of docked SVs along the active zone membrane, i.e. their distribution relative to the DP (**Fig. 5F**). In non-stimulated synapses, docked SVs were most frequently found in close proximity to the DP, i.e. within 33 nm, and this leveled off to baseline between 132 and 165 nm distal to the DP. *rimb-1* mutants contained significantly fewer docked SVs in the 33 nm bin, but did not differ from wild type at other distances. This indicated that docked SVs distributed more distally in *rimb-1* mutants, possibly because SV tethering with the UNC-10/RIM scaffold is compromised (evident also from a cumulative distribution analysis; **Fig. S7B**). Upon photostimulation, wild type synapses fused SVs most effectively in close proximity to the DP, while in *rimb-1* mutants this occurred more distal to the DP (**Fig. 5F inset, Fig. S7B**). This is in line with putative mislocalization of UNC-2 VGCCs in *rimb-1* mutants, e.g. more distal to the DP, where SVs may experience a higher Ca^{2+} concentration than at the DP.

Untethering P/Q type VGCCs affects transmission and counteracts the loss of RIMB-1

VGCCs are tethered to docked SVs by RIM and RIMB-1 via multiple interactions, involving the SH3 and PDZ domains of RIMB-1 and RIM, respectively, which bind the UNC-2/Ca_v2 C-terminus (**Fig. 1B, 6A**). Thus far, we either analyzed the mild defect induced by the loss of RIMB-1 (or, its second SH3 domain) in the *tm5964* allele, or the very strong defect induced by loss of UNC-10/RIM. Phenotypes of the latter likely are strong because they involve additional functions of RIM, not only UNC-2 tethering. We reasoned that untethering the UNC-2 channel by eliminating its C-terminal 10 amino acids may achieve an intermediate phenotype and exacerbate the *rimb-1* phenotype, when combined, allowing UNC-2 to diffuse even more. We thus removed the UNC-2 PDZ ligand by CRISPR-mediated genome editing, from now on referred to as UNC-2-ΔPDZ. As a means to acutely eliminate UNC-2 function, and to phenotypically compare this to completely untethering UNC-2, we used a photosensitive degron (PSD) (Hermann et al., 2015). The PSD was fused to the C-terminus of the essential VGCC β-subunit CCB-1 by CRISPR-editing (**Fig. 6B**), which is required for VGCC biogenesis and function (Laine et al., 2011). The PSD can effectively degrade synaptic proteins within 45-60 min of mild blue illumination. This manipulation is expected to disrupt the CCB-1 protein and to either inactivate the VGCC complex, or to destabilize it and cause its degradation.

First, we analyzed cholinergic transmission in UNC-2-ΔPDZ animals and in *rimb-1*; UNC-2-ΔPDZ double mutants (**Fig. 6C**). UNC-2-ΔPDZ per se had no phenotype in the aldicarb assay, however, it appeared to counteract rather than exacerbate the resistance phenotype of *rimb-1* mutants. UNC-2-ΔPDZ animals were slightly, but significantly affected for swimming, but again, the *rimb-1*; UNC-2-ΔPDZ double mutants were somewhat rescued when compared to the *rimb-1* mutants, and this was similarly found for ChR2-evoked body contractions (**Fig. 6D; S8B**). Next, we analyzed synaptic transmission by electrophysiology in UNC-2-ΔPDZ and *rimb-1*; UNC-2-ΔPDZ animals, before and during photostimulation of cholinergic neurons (**Fig. 6E-J**). Spontaneous release (mPSC rate) was not significantly reduced in UNC-2-ΔPDZ animals, and reverted (in the double mutant) the significantly reduced mPSC rate of *rimb-1* animals (**Fig. 6E**), while mPSC amplitudes were not altered.

In sum, untethering of UNC-2 is not strongly deleterious for spontaneous activity, and it may allow the VGCC to trigger SVs that it cannot efficiently reach in the *rimb-1* mutant, when it is still tethered to UNC-10/RIM. However, UNC-2-ΔPDZ animals exhibited more strongly reduced ePSC amplitudes when compared to *rimb-1* mutants and to wild type (**Fig. 6F**), indicating that UNC-2-ΔPDZ supports spontaneous release, but fails to do so during evoked activity. Possibly, the strong optogenetic stimulus requires tight coupling of UNC-2 and docked SVs. UNC-2-ΔPDZ and particularly *rimb-1*; UNC-2-ΔPDZ double mutants, were delayed in their time to peak (**Fig. 6G, I, J**), in line with an increased distance of the VGCC to the docked SV, while the rise time was unaffected. Quantal content was unaltered in this set of mutants (**Fig. 6H**).

We compared effects of untethering vs. absence of UNC-2. In *unc-2(ra612)* loss-of-function mutants, mPSC frequency was largely reduced, but mPSC amplitude was unaltered (**Fig. 6K**), similar to the UNC-2-ΔPDZ mutant and the *rimb-1*; UNC-2-ΔPDZ double mutants (**Fig. 6E; S8C**). In contraction assays, *unc-2(ra612)* mutants showed largely reduced effects and were most similar to *rimb-1(tm5964)* mutants (**Fig. S8A, B**). Because these mutations may induce long-lasting compensatory effects, we analyzed the acute depletion of the VGCC β-subunit CCB-1. 1 h photodegradation of CCB-1::PSD caused aldicarb resistance, though only in the absence of GABAergic signaling in *unc-47* mutants (likely because of an excitation-inhibition imbalance in the CCB-1::PSD strain; **Fig. 6L**). Furthermore, it significantly reduced swimming, compared to illuminated wild type animals, and this effect recovered after 24h (**Fig. 6M**). The mPSC frequency was significantly decreased by about 75% in CCB-1::PSD animals after 1h blue light illumination, confirming acute degradation of CCB-1, yet did not significantly affect mPSC amplitude (**Fig. 6N**). Thus, UNC-2 function is affected by the acute absence of the CCB-1 β-subunit, either through an effect on channel properties, or by affecting stability of the channel in the plasma membrane, or both. In sum, depending on the assay, untethering of Ca_v2/UNC-2 had specific phenotypes opposing those of the absence of RIMB-1, which it could partially balance, and was similar to the complete loss of function of UNC-2. Since the latter does not eliminate all transmission, this implies that other VGCCs compensate for function at the NMJ, most likely EGL-19 L-type VGCCs, as shown previously (Liu et al., 2018).

UNC-2/Ca_v2 synaptic density is reduced in the absence of RIMB-1 or the β-subunit

The de-anchoring of the UNC-2 channel via elimination of the RIMB-1 protein and the PDZ ligand at the UNC-2 C-terminus affect (i.e. increase) its mobility in the synapse, and thus likely diminish its location in vicinity of docked SVs (i.e. move it away, on average). Yet, it

may also affect its stabilization in the active zone membrane. This was addressed by fluorescence microscopy, using a strain with a GFP sequence inserted by CRISPR in-frame in the N-terminal domain of UNC-2 (a gift of Mei Zhen; Gao et al., 2018), to image GFP::UNC-2 in nerve ring synapses (**Fig. 7A**). We further deleted the UNC-2 PDZ ligand in this strain, and compared both strains in wild type and *rimb-1(tm5964)* background, assessing overall nerve ring fluorescence level (**Fig. 7B**) as well as synaptic puncta intensity and size (**Fig. 7C, D**).

Fluorescence levels were significantly reduced in animals lacking both RIMB-1 and the UNC-2 PDZ ligand, compared to all other genotypes. This could be due to less clustering, or to overall reduction of the (synaptic) expression level of the VGCC α-subunit UNC-2. The fluorescence intensity of UNC-2 clusters was also significantly reduced without RIMB-1, and even more so by the additional deletion of the UNC-2 PDZ ligand. Cluster size was not significantly different. Thus, loss of RIMB-1 and UNC-2 anchoring leads to reduced synaptic levels of the channel, which may explain the reduced synaptic function. Alternatively, UNC-2 does not traffic efficiently to the synapse, or its localization is more diffuse. To shed more light on the effects of acute reduction of channel stability, we analyzed GFP::UNC-2 in the presence or absence of CCB-1::PSD, i.e., following its photodegradation. GFP::UNC-2 and CCB-1::mKate2::PSD mostly co-localized in synaptic puncta, although CCB-1 was more abundant and present also at more peripheral regions of synapses (**Fig. 7C**). Fluorescence of CCB-1::mKate2::PSD was significantly reduced after 1 h of blue illumination (**Fig. 7D**), while GFP::UNC-2 signal was not affected by the same blue light treatment (**Fig. 7E**). However, combination with CCB-1::PSD reduced GFP::UNC-2 levels in the dark, and, even more, in response to blue light. Thus, absence of the β-subunit affected UNC-2 function and synaptic density in a similar way as the absence of RIMB-1 and the UNC-2 PDZ ligand, most likely affecting the close proximity of the P/Q-type VGCC to docked SVs.

Discussion

The fidelity and robustness of synaptic transmission depends on the precise morphology and spatial organization of the active zone (Sudhof, 2013). Thus, mutations in proteins that orchestrate the anchoring and tight apposition of docked SVs and Ca_v2 VGCCs are likely to negatively affect this process. Also, such proteins are probable targets for regulation of synaptic transmission, and could be utilized to set the excitation-inhibition balance also in complex neural circuits (Huang et al., 2019; Liu et al., 2018). Here, we characterized in detail the function of the *C. elegans* RIMB-1 protein, as well as its (functional) interaction with the Ca_v2/UNC-2 VGCC, and determinants of VGCC localization at NMJ synapses, in cholinergic and GABAergic neurons.

The lack of RIMB-1 function in *C. elegans* synapses had a mild phenotype on behavior (swimming) and caused some resistance to the ACh esterase inhibitor aldicarb, demonstrating cholinergic deficits. In response to optogenetic stimulation, the defect was also observable, however, lack of UNC-10/RIM had much more severe defects. The phenotypes of the double mutant were dominated by the *unc-10* defects, somewhat contradictory to an earlier report (Kushibiki et al., 2019), that assessed UNC-2::GFP overexpressed from a transgene. Thus, the situation in worms differs from that of the *Drosophila* NMJ, where *drbp* mutants had more severe phenotypes than *rim* mutants, depending on whether baseline or plasticity inducing conditions are studied (Liu et al., 2011; Muller et al., 2015).

Electrophysiology surprisingly showed increased transmission in *rimb-1* mutants in response to cholinergic stimulation. However, voltage imaging demonstrated the reduced depolarization in *rimb-1* animals, in line with the behavioral defects. We could clarify that this is likely due to the combined effect of cholinergic and GABAergic transmission, which are co-stimulated by ChR2 in cholinergic neurons. Depending on the configuration of the experiment, and whether the circuit as a whole is probed, or only GABAergic neurons, a summed (reduced) response is observed, while direct photostimulation of GABAergic neurons revealed no deficit in behavioral assays, despite reduced GABA ePSCs (**Fig. 8**). Overall, our findings show a differential importance of RIMB-1 in cholinergic vs. GABAergic synapses. Such differential functions were also found in different central synapses in the mouse (Brockmann et al., 2019). In *C. elegans*, a gain-of-function mutation in UNC-2/Ca_v2 was recently shown to induced increased cholinergic transmission but a reduction in GABA transmission through effects on $GABA_A$ receptors, or rather, GABA synapse numbers (Huang et al., 2019). Here, we probed post-synaptic nAChRs through levamisole paralysis assays, which did not show a defect in *rimb-1* mutants. We probed GABAergic synapses by direct ChR2-induced stimulation, which showed reduced currents in *rimb-1* mutants (**Fig. 3L**). Spontaneous GABA transmission showed reduced frequency but unaltered amplitudes in *rimb-1* animals (**Fig. S6**), which could be explained with reduced GABA synapse numbers. An additional layer of complexity at the *C. elegans* NMJ is given by the feedback inhibition that GABAergic neurons can elicit to cholinergic motor neurons via the AVA premotor interneurons (Liu et al., 2020). Also this way, reduced synaptic transmission due to the lack of RIMB-1 may affect the summed outcome of NMJ transmission in intact animals, but maybe less in electrophysiology, where commissural connections important for this feedback may be severed during dissection.

Mislocalization of Ca_v2/UNC-2 leads to lower ACh release as fewer SVs are accessed by Ca^{2+}, as is supported by our analysis of spontaneous release (mPSCs; **Fig. 3A, C**), and in behavioral assays (**Fig. 2**). However, if Ca_v2/UNC-2 channels can rather freely diffuse in the synaptic membrane, they may also affect SVs that are docked in regions where they would normally not fuse. When optogenetic stimulation is used, which is much stronger than physiological activity during spontaneous release (Liewald et al., 2008; Liu et al., 2009), the larger Ca^{2+} domains could reach more docked SVs, distal to the active zone, where fusion events can still be observed (Watanabe et al., 2013). This may slow down transmission, though. As in other systems, RIMB-1 function is required for faithful and fast transmission (Acuna et al., 2016), as the time from an optogenetic stimulus to reaching ePSC peak was delayed in both cholinergic and GABAergic *rimb-1* mutant synapses. Quantal content was not reduced in *rimb-1* mutants, thus even if fewer SVs were released in a fast manner, overall the synapse was able to fuse normal numbers of SVs, only over a prolonged time. This indicates that Ca^{2+} levels in the vicinity of SVs rise more slowly in *rimb-1* mutants, but eventually reach sufficient levels to fuse SVs. However, the site of release was more remote from the dense projection, likely because Ca_v2/UNC-2 channels moved to more distal positions relative to the DP in the active zone membrane. The deletion of the C-terminal PDZ ligand of the UNC-2 channel, by which it is anchored to RIM, had in part similar effects as the *rimb-1* mutation (mPSC frequency), in part it was less (behavior), or more severe (ePSC amplitude, evoked body contraction). In combination, the phenotypes of *rimb-1* and UNC-2-ΔPDZ were exacerbated or counteracted each other. This is not easy to reconcile, but may again be explained by the different degree of UNC-2/Ca_v2 de-anchoring, and the complex signaling in the motor circuit, spontaneous versus evoked activity and the need for precise VGCC localization for the latter. The photodegradation of the CCB-1::PSD β-subunit, which

strongly reduced mPSC frequency, and thus likely induced an acute functional elimination of the Ca_v2 channel complex, had a similar effect as its de-anchoring. Both manipulations led to a similar reduction in GFP::UNC-2 signal at nerve ring synapses, which may be due to destabilization and partial loss of the channel; yet also a re-localization away from synaptic regions into the axonal plasma membrane appears possible. To rigorously distinguish these possibilities, immunogold localization or super-resolution imaging would be required.

Recently, the effect of eliminating all Ca_v2 channels on synapse structure was analyzed in mammalian synapses (Held et al., 2020). Overall synapse structure was not affected, although the Ca_v2 β-subunit lost its localization to synaptic regions. This is in line with our findings, where loss of CCB-1 may also affect UNC-2 synaptic location, thus these proteins may mutually influence each other. The authors also analyzed the deletion of the entire C-terminus of murine $Ca_v2.1$, which demonstrated that it is required for channel targeting to the synapse, and for triggering of efficient SV release. However, in mice, removing only the C-terminal PDZ ligand had no effects on its own (unlike in *C. elegans*), but had to be combined with removal of the Ca_v2 RIM-BP binding site to evoke effects. This latter situation resembles our combination of *rimb-1* and UNC-2-ΔPDZ. Another study of the $Ca_v2.1$ C-terminus, however, did not observe alterations in VGCC function in mice when the RIM and RIM-BP binding sites were simultaneously removed (Lubbert et al., 2017). Thus, there may be species-specific differences in the regulation of the Ca_v2 channel and its synaptic localization by binding partners.

Overall our work confirms the general evolutionary conservation of RIM-BP function in *C. elegans*, and provides new information on how the protein regulates synaptic transmission through accurate placing of Ca_v2 channels in the vicinity of docked SVs. It further provides information on how this protein may also be used to set excitation-inhibition balance in complex circuits, by differentially affecting each synapse type, in this case cholinergic and GABAergic motor neurons. In the future, cell-type specific determinants of RIMB-1 function, e.g. through posttranslational modification or changes in expression level, will have to be revealed. Our work lays ground for such approaches and provides guidelines for similar analyses at the circuit level in higher animals.

Materials and Methods

Strains

C. elegans wild type Bristol N2 and mutant strains were maintained on NGM plate seeded with *E. coli* OP50 as described earlier (Brenner, 1974). Young adult hermaphrodites cultured at 20°C were used. Mutant alleles and integrated transgenes used in this study:

rimb-1(tm5964)
CB307: *unc-47(e307)*
NL735: *unc-2(pk95::Tc1)X*
NM1657: *unc-10(md1117)*
ZM9583: *unc-2(hp858[GFP::UNC-2])* (GFP knock-in in genomic location of *unc-2*)
ZX426: *zxIs3[punc-47::ChR2(H134R)::yfp; lin-15+]*
ZX460: *zxIs6[punc-17::ChR2(H134R)::yfp; lin-15+]V*
ZX531: *unc-47(e307)III; zxIs6[punc-17::ChR2(H134R)::yfp; lin-15+]*
ZX1605: *unc-2(pk95::Tc1)*; *zxIs6[punc-17::ChR2(H134R)::yfp; lin-15+]*

ZX1954: *zxIs120[pmyo-3::Arch(D95N)::2xmyc; pmyo-3::CFP]; zxIs6[punc-17::ChR2(H134R)::yfp; lin-15+]*
ZX2025: *rimb-1(tm5964)III; zxIs6[punc-17::ChR2(H134R)::yfp; lin-15+]*
ZX2271: *ccb-1(zx3[ccb-1::mKate2::PSD])* (CRISPR knock-in of mKate2 with a photosensitive degron (PSD))
ZX2320: *ccb-1(zx3[ccb-1::mKate2::PSD]); zxIs5[punc-17::ChR2(H134R)::yfp; lin-15+]*
ZX2321: *ccb-1(zx3[ccb-1::mKate2::PSD]); unc-2(hp858[GFP::UNC-2])*
ZX2340: *unc-10(md1117); rimb-1(tm5964)*
ZX2412: *unc-10(md1117); rimb-1(tm5964); zxIs6[punc-17::ChR2(H134R)::yfp; lin-15+]*
ZX2413: *unc-10(md1117); zxIs6[punc-17::ChR2(H134R)::yfp; lin-15+]*
ZX2474: *zxEx1137[primb-1::GFP; punc-17::mCherry]*
ZX2574: *rimb-1(tm5964)III; zxIs3[punc-47::ChR2(H134R)::yfp; lin-15+]*
ZX2562: *rimb-1(tm5964)III; oxIs353[pmyo-3::ChR2::mCherry::unc-54 3'-UTR; lin15+]V*
ZX2573: *ccb-1(zx3[ccb-1::mKate2::PSD]); unc-47(e307) III.*
ZX2584: *rimb-1(tm5964); zxIs120[pmyo-3::Arch(D95N)::2xmyc; pmyo-3::CFP]; zxIs6[punc-17::ChR2(H134R)::yfp; lin-15+]*
ZX2623/PHX1749: *unc-2(syb1749[UNC-2-ΔPDZ])* (UNC-2-ΔPDZ CRISPR deletion of 10 C-terminal amino acids)
ZX2624: *unc-2(syb1749[UNC-2-ΔPDZ]); zxIs6[punc-17::ChR2(H134R)::yfp; lin-15+]*
ZX2625: *unc-2(syb1749[UNC-2-ΔPDZ]); rimb-1(tm5964)III; zxIs6[punc-*ZX2626: *rimb-1(tm5964)III; unc-47(e307)III; zxIs6[punc-17::ChR2(H134R)::yfp; lin-15+]*
ZX2627: *snb-1(md247)V; oxIs353[pmyo-3::ChR2::mCherry::unc-54 3'-UTR; lin15+]V*
ZX2691: *unc-2(syb2088[UNC-2-ΔPDZ]); unc-2(hp858[GFP::UNC-2])*
ZX2757: *unc-2(syb1749[UNC-2-ΔPDZ])* 3x outcrossed
ZX2758: *unc-2(syb1749[UNC-2-ΔPDZ]); zxIs6[punc-17::ChR2(H134R)::yfp; lin-15+]*
ZX2759: *unc-2(syb1749[UNC-2-ΔPDZ]); rimb-1(tm5964)III; zxIs6[punc-17::ChR2(H134R)::yfp; lin-15+]*
ZX2691/PHX2088: *unc-2(syb2088[UNC-2-ΔPDZ]); unc-2(hp858[GFP::UNC-2])* (UNC-2-ΔPDZ CRISPR deletion of 10 C-terminal amino acids in GFP::UNC-2 insertion)
ZX2824: *rimb-1(tm5964) III; unc-2(syb2088[UNC-2-ΔPDZ]); unc-2(hp858[GFP::UNC-2])*
ZX2825: *rimb-1(tm5964) III; unc-2(hp858[GFP::UNC-2])*

Molecular biology

To investigate the expression pattern of RIMB-1, we created *a rimb-1p::GFP* plasmid. The *rimb-1* promoter (3 kb upstream of ATG) was amplified by PCR from genomic DNA using primers oBJ76 (TAGCTCTTCCAGCGAGAGGACCTCCTCCTC) and oBJ77 (AGCGCTGTTGGTGACTAGGTGGTCC), was inserted into vector pCS179 (*flp-1p(trc)::GFP*) containing GFP, described in Oranth et al., 2018.

The strain ZX2271 *(ccb-1(zx3[ccb-1::mKate2::PSD]))* was generated using a CRISPR knock-in strategy (Dickinson et al., 2015). The *C. elegans* germline was injected with a plasmid that serves as a template to transcribe a guide RNA (gRNA) that targets the C-terminus-encoding sequence of *ccb-1.* The gRNA binding sequence (AAGAGGTACGTACAGGTACT) was inserted into the vector pDD162 (from Addgene) using the NEB Q5 Site-Directed Mutagenesis Kit. A second plasmid (pIA03) was co-injected in the germline to serve as a repair template, which includes the sequences for fluorescent protein mKate2, PSD, and a self-excising cassette containing a dominant visible marker for a rolling phenotype (*sqt-1(d))*, a heat shock-inducible Cre recombinase *(hs::Cre)*, and hygromycin resistance gene *(hygR)*. The progenies of injected animals were selected for hygromycin resistance and rolling phenotype. Animals were then heat shocked (34°C for 4 hours) to excise the cassette, thus ending up with the *ccb-1::mKate2::PSD* sequence only. Successful knock-in was verified by PCR (forward primer: GGGGGTACGCACATTACTG, reverse primer

GGGGATGTCACAAAACGGGCTG) and Sanger sequencing (primer: GCAGCAACCACAACAGCAACAAC).

Behavioral assays

Transgenic worms were cultivated in the dark at 20°C on nematode growth medium (NGM) with OP50-1 bacteria (Brenner, 1974) without or with all-*trans* retinal (ATR; Liewald et al., 2008). Dishes containing ATR were prepared by spreading 320 µl of OP50-1 culture, mixed with 0.64 µl of 100 mM ATR stock (dissolved in ethanol) onto 5.5-cm dishes containing 8.2 ml of NGM. About 18 h prior to the experiments, L4 larvae, grown on ATR plates, were placed on fresh ATR plates. Worms were illuminated with blue light (contraction-assay: 1.4 mW/mm^2, swimming-assay: 0.53 mW/mm^2) from a 50 W HBO mercury lamp, filtered through a GFP excitation filter (450–490 nm), on 5.5 cm diameter dishes, under a 10× objective in a Zeiss Axiovert 40 microscope (Zeiss, Germany). The duration of illumination was defined by a computer-controlled shutter (Sutter Instruments). Worms were filmed with a Powershot G9 digital camera (Canon, Japan) at 640 × 480 resolution with 30 fps. The body length was determined as previously described (Erbguth et al., 2012). The length values were normalized to the averaged values measured before illumination (0–5 s; normalization was carried out for each animal). To exclude measurement errors (i.e. when the animals body touches itself), all values below 80% were excluded and the length-profiles were averaged for each strain. The experiments were repeated on 2–3 different days (worms were picked from different populations); the final graphs show the average of all individual animals.

For analyzing swimming behavior, worms were placed into 96-well plates containing 100 µl NGM and 100 µl of M9 buffer per well. For analysis of the effect of CCB-1 photodegradation, animals were illuminated for 1h (470 nm, 400 µW, 20°C). Worms were left in M9 buffer for 15 min before the swimming-assay, then they were filmed for 60 s. The swimming cycles (the animals' body bends twice per cycle), were counted manually. The swimming assays were repeated on three different days, with 9–10 worms/group, picked from different populations.

Pharmacological (Aldicarb and Levamisole) Assays

To assay aldicarb sensitivity, 1.5 mM aldicarb dishes were prepared (Mahoney et al., 2006). After transferring the animals (14–15 young adults/trial, in total three trials on three different days, with worms picked from different populations) to the dishes, they were scored every 30 min by three gentle touches with a hair pick. The assays were performed blinded and on the same day with the same batch of aldicarb dishes. For analysis of the effect of CCB-1 photodegradation, animals were illuminated for 1h (470 nm, 100 µW, 1h, 20°C), and then incubated on 1 mM aldicarb plates. The data for the 1.5 and 2 h time points were averaged.

For levamisole assays, we used an agonist of the levamisole-sensitive nAChR of the neuromuscular junction, the racemic mixture tetramisole, at 2 mM on NGM plates (corresponding to 1 mM levamisole). Animals were incubated on these plates as described for the aldicarb assay, and assessed for paralysis every 30 min.

Electrophysiology

Electrophysiological recordings from body wall muscle cells were conducted in immobilized and dissected adult worms as described previously (Liewald et al., 2008). Animals were immobilized with Histoacryl glue (B. Braun Surgical, Spain) and a lateral incision was made to access neuromuscular junctions (NMJs) along the anterior ventral nerve cord. The basement membrane overlying body wall muscles was enzymatically removed by incubation in 0.5 mg/ml collagenase for 10 s (C5138, Sigma-Aldrich, Germany). Integrity of body wall

muscle cells and nerve cord was visually examined via DIC microscopy. Recordings from body wall muscles were acquired in whole-cell patch-clamp mode at room temperature (20-22°C) using an EPC-10 amplifier equipped with Patchmaster software (HEKA, Germany). The head stage was connected to a standard HEKA pipette holder for fire-polished borosilicate pipettes (1B100F-4, Worcester Polytechnic Institute, Worcester, MA, USA) of 4-9 MΩ resistance and recordings were sampled at 3.33 kHz.

The extracellular bath solution consisted of 150 mM NaCl, 5 mM KCl, 5 mM $CaCl_2$, 1 mM $MgCl_2$, 10 mM glucose, 5 mM sucrose, and 15 mM HEPES (pH 7.3 with NaOH,~330 mOsm). The internal/patch pipette solution consisted of K-gluconate 115 mM, KCl 25 mM, $CaCl_2$ 0.1 mM, $MgCl_2$ 5 mM, BAPTA 1 mM, HEPES 10 mM, Na_2ATP 5 mM, Na_2GTP 0.5 mM, cAMP 0.5 mM, and cGMP 0.5 mM (pH 7.2 with KOH,~320 mOsm). With the solutions used, reversal potentials are about +20 mV for nicotinic ACh receptors (nAChRs) and -30 mV for $GABA_A$ receptors (Maro et al., 2015). For most experiments, recordings were conducted at a holding potential of −60 mV where nAChR-related currents (EPSCs) and $GABA_A$ receptor-related currents (IPSCs) both display as inward currents. At a holding potential of -10 mV (**Fig. S6A**), however, EPSCs and IPSCs are recorded as inward and outward currents, respectively.

Light activation was performed using an LED lamp (KSL-70, Rapp OptoElectronic, Hamburg, Germany; 470 nm, 8 mW/mm²) and controlled by the Patchmaster software. Subsequent analysis and graphing was performed using Patchmaster, and Origin (Originlabs). Analysis of mPSCs was conducted with MiniAnalysis (Synaptosoft, Decatur, GA, USA, version 6.0.7) to acquire parameters such as mPSC frequency, peak amplitude, time to peak (time from start of light stimulus until peak maximum), rise time (time from start of peak until peak maximum), decay time, and area under the curve. For the analysis of quantal content, the area under the curve of photo-evoked currents was divided by the mean area under the curve of respective mPSCs of the same animal measured before photostimulation.

Fluorescence Microscopy

For analyzing the fluorescence level of GFP::UNC-2 and CCB-1::mKate2::PSD in the nerve ring, animals were transferred onto 10% agarose pads in M9 buffer (K_2PO_4 20 mM; Na_2HPO_4 40 mM; NaCl 80 mM; $MgSO_4$ 1 mM) and immobilized with 1 µl 20 mM tetramisole hydrochloride. For the widefield fluorescence imaging of these animals, an Axiovert 200 or an Observer Z1 microscope (Zeiss, Germany) was used, equipped with a 40x/1.3 Zeiss oil objective, a 460 nm LED (Prior Scientific), a GFP filter cube (ex. 470/40 nm, em. 520/35 nm) and RFP filter cube (ex. 580/23 nm, em. 625/15). The nerve ring region was located using white transmission light. The fluorescence excitation light was turned on and a fluorescence image was captured using an EMCCD camera (Photometrics Evolve 512 Delta), gain (GFP: 68 (ZM9583), 4 (ZX2321); RFP: 20 (ZX2321, ZX2271), exposure time 50 ms (ZM9583) or 100 ms (ZX2321, ZX2271), controlled using Micro Manager software (Edelstein et al., 2014). Images were analysed using FIJI software (Schindelin et al., 2012). For quantification, a ROI was placed around the nerve ring and mean fluorescence intensity was measured. For background correction, a background value was measured in the worm's head close to the nerve ring.

Confocal Microscopy

The expression patterns of *rimb-1p*::GFP and *unc-17p::mCherry* (strain ZX2474) were analyzed using a spinning disc confocal microscope (Cell Observer SD, Zeiss, Germany), equipped with a 40x air objective (LD Plan-NEOFLUAR 40x/0.6 PH2 Kor ∞/0 1,5; Zeiss, Germany), an LED-based illumination system (excitation wavelengths 488 nm and 561 nm)

and a double band pass emission filter (DBP 527/54 + 645/60, Zeiss). Micrographs were taken with an EMCCD camera (Rolera EM-C2, Teledyne QImaging). Animals were transferred onto 10% agarose pads in M9 buffer and immobilized with Polybead polystyrene 0.1 mm microspheres (Polysciences Inc., Warrington, PA, USA).

For analyzing the synaptic puncta intensity and size of GFP::UNC-2 in the nerve ring, animals were immobilized as described above (10% agarose pads in M9; 1 µl 20 mM tetramisole hydrochloride). In this case the spinning disc confocal microscope (Cell Observer SD, Zeiss, Germany), was equipped with a 63 x oil immersion objective (63 x/ 1.4 Oil DIC Plan apochromat), LED illumination (488 nm) and a 520/35 nm emission filter. Gain (150) and exposure time (1000 ms) were controlled by ZEN 2 blue software (Zeiss). Images were obtained with a Rolera EM-C2 EMCCD camera (Teledyne QImaging). After locating the nerve ring using only white light, z-stacks were acquired using a piezo focused stage (NanoScan Z, Prior Scientific). 40 images (0.5 µm spacing) were taken per animal, which were then z-projected (standard deviation) and analysed using FIJI software.

Electron Microscopy

Transgenic L4 worms were transferred from regular NGM dishes to freshly seeded E. coli OP50 −/+ (0.1 mM) ATR dishes 1 to 2 days before high-pressure freezing (HPF). Young adult animals were used for HPF fixation, based on methods previously described (Rostaing et al., 2004; Weimer, 2006; Kittelmann et al., 2013). Briefly, about 10–40 worms were loaded into a 100 µm deep aluminum planchette (Microscopy Services) filled with *E. coli* OP50 −/+ ATR, covered with a 0.16 mm sapphire disc and a 0.4 mm spacer ring (Engineering Office M. Wohlwend GmbH) for subsequent photostimulation. To prevent preactivation, all manipulations were done under red light. For light stimulation experiments, worms were continuously illuminated with a laser (~20 mW/mm^2) for 30 s, followed by HPF at −180°C under 2100 bar pressure in a Bal-Tec HPM010 HPF machine. A ~5 s period of manual insertion of the sample after photostimulation is required with this high pressure freezer.

After freezing, specimens were transferred under liquid nitrogen into a Reichert AFS machine (Leica) for freeze substitution. Tannic acid (0.1% in dry acetone) fixative was used to incubate samples at −90°C for 100 h. Then, a process of washing was performed, followed by an incubation of 2% OsO_4 for 39.5 h (in dry acetone) while slowly increasing the temperature up to room temperature. Afterwards, the process of embedding in Epoxy resin (Agar Scientific, AGAR 100 Premix kit hard) was executed with increasing concentration from 50% to 100% at room temperature and 100% at 60°C over 48 h.

For electron micrographs, cross sections were cut at a thickness of 40 nm, transferred to formvar-covered copper slot grids and counterstained in 2.5% aqueous uranyl acetate for 4 min, followed by washing with distilled water. Then, grids were carried onto Reynolds lead citrate solution for 2 min in a CO_2-free chamber and subsequently washed in distilled water again. Images of regions in the ventral nerve cord were taken with an Erlangshen ES500W CCD camera (Gatan) in a Philips CM12 transmission electron microscope operated at 80 kV. Images were scored blind for each condition and tagged in ImageJ (NIH). ImageJ ROIs were stored and then quantified based on methods described previously (Steuer Costa et al., 2017). The diameters of synapses from each stimulation condition vary due to the different extent of SV exocytosis or because different synapses were sampled. Thus, each value for the number of docked SVs was normalized and represents the number of docked SVs along a membrane whose perimeter is 1548 nm in a profile; the other organelles are represented as the numbers of SVs or LVs in a typical synaptic profile of 164,100 nm^2 (Steuer Costa et

al., 2017). SV size was scored from 3 to 10 middle images of randomly selected synapses or from randomly selected single images per synapse for each mutant or stimulation protocol. 2–3 worms, and typically 10–19 synapses were analyzed per genotype and condition; 1–2 technical replicates were performed.

Voltage imaging

For voltage imaging experiments, ATR (Sigma-Aldrich, USA) had to be supplied to the animals. Therefore, one day prior to each experiment, transgenic L4 stage worms were transferred onto NGM plates, seeded with OP50 bacterial suspension supplemented with ATR (final ATR concentration: 0.01 mM). For imaging, animals were immobilized with polystyrene beads (0.1 µm diameter, at 2.5% w/v, Sigma-Aldrich) on top of 10 % agarose pads (in M9 buffer). Voltage-dependent fluorescence of Arch(D95N) was excited with a 637 nm red laser (OBIS FP 637LX, Coherent) at 1.8 W/mm^2 and imaged at 700 nm (700/75 ET bandpass filter, integrated in Cy5 filter cube, AHF Analysentechnik), while ChR2(H134R) was stimulated by a monochromator (Polychrome V) at 300 µW/mm^2. Imaging was performed on an inverted microscope (Zeiss Axio Observer Z1), equipped with a 40x oil immersion objective (Zeiss EC Plan-NEOFLUAR 40x/ N.A. 1.3, Oil DIC ∞ / 0.17), a laser beam splitter (HC BS R594 lambda/2 PV flat, AHF Analysentechnik), a galilean beam expander (BE02-05-A, Thorlabs) and an EMCCD Camera (Evolve 512 Delta, Photometrics).

Statistical Analysis

All quantitative data were reported as mean ± s.e.m., and n indicated the number of animals, N the number of replicates. Significance between data sets after two-tailed Student's t-test or after one-way or two-way ANOVA, with Bonferroni's multiple comparison test, Fisher test, or Tukey's post-hoc test, is given as p-value. If data was not distributed normally, we used Newman-Keuls test, or Kruskall-Wallis test with Dunn's multiple comparisons. For paralysis assays, we used the log rank test (with Bonferroni correction) to compare datasets across the duration of the experiment. The respective statistics used are indicated for each experiment in the figure legends. * signifies $p<0.05$, **$p<0.01$, and ***$p<0.001$. Data was analyzed and plotted in GraphPad Prism (GraphPad Software, Inc., La Jolla, CA, USA, version 8.02), Microsoft Excel 2016, or in OriginPro 2020b (OriginLab Corporation, Northampton, USA).

Acknowledgements

We thank members of the Gottschalk lab for critically reading the manuscript. We acknowledge the *Caenorhabditis* Genetic Center, which is funded by NIH Office of Research Infrastructure Programs (P40 OD010440), and the National Bioresource project, nematode *C. elegans*, for strains. We further thank Mei Zhen, Erik Jorgensen and Bob Goldstein for additional strains and transgenes, and Daniel J. Dickinson for advice on CRISPR gene editing. We are indebted to Franziska Baumbach, Hans-Werner Müller, Heinz Schewe and Mona Hoeret for expert technical assistance. This work was supported by grants from the Deutsche Forschungsgemeinschaft (DFG), grants CRC1080-B02 and CRC807-P11, to A.G., and by Goethe University Frankfurt. Ivan C. Alcantara was a Fulbright scholar.

Author contributions

Experiments were conceived, designed, and analyzed by B.J., J.F.L., S.-c. Y., S.U., I.C.A., A.C.F.B., M.W.S., and A.G. Experiments were conducted by B.J., J.F.L., S.-c. Y., S.U., I.C.A., A.C.F.B., M.W.S., and J.S. The manuscript was written by B.J., J.F.L., and A.G. Funding was acquired by A.G.

Declaration of Interests

The authors declare no competing interests.

References

Ackermann, F., Waites, C.L., and Garner, C.C. (2015). Presynaptic active zones in invertebrates and vertebrates. EMBO Rep *16*, 923-938.

Acuna, C., Liu, X., Gonzalez, A., and Sudhof, T.C. (2015). RIM-BPs Mediate Tight Coupling of Action Potentials to Ca(2+)-Triggered Neurotransmitter Release. Neuron *87*, 1234-1247.

Acuna, C., Liu, X., and Sudhof, T.C. (2016). How to Make an Active Zone: Unexpected Universal Functional Redundancy between RIMs and RIM-BPs. Neuron *91*, 792-807.

Azimi Hashemi, N., Bergs, A.C.F., Schuler, C., Scheiwe, A.R., Steuer Costa, W., Bach, M., Liewald, J.F., and Gottschalk, A. (2019). Rhodopsin-based voltage imaging tools for use in muscles and neurons of Caenorhabditis elegans. Proc Natl Acad Sci U S A *116*, 17051-17060.

Brenner, S. (1974). The genetics of Caenorhabditis elegans. Genetics *77*, 71-94.

Brockmann, M.M., Maglione, M., Willmes, C.G., Stumpf, A., Bouazza, B.A., Velasquez, L.M., Grauel, M.K., Beed, P., Lehmann, M., Gimber, N.*, et al.* (2019). RIM-BP2 primes synaptic vesicles via recruitment of Munc13-1 at hippocampal mossy fiber synapses. eLife *8*.

Brockmann, M.M., Zarebidaki, F., Camacho, M., Grauel, M.K., Trimbuch, T., Sudhof, T.C., and Rosenmund, C. (2020). A Trio of Active Zone Proteins Comprised of RIM-BPs, RIMs, and Munc13s Governs Neurotransmitter Release. Cell reports *32*, 107960.

Brunger, A.T., Choi, U.B., Lai, Y., Leitz, J., and Zhou, Q. (2018). Molecular Mechanisms of Fast Neurotransmitter Release. Annual review of biophysics *47*, 469-497.

Dickinson, D.J., Pani, A.M., Heppert, J.K., Higgins, C.D., and Goldstein, B. (2015). Streamlined Genome Engineering with a Self-Excising Drug Selection Cassette. Genetics *200*, 1035-1049.

Edelstein, A.D., Tsuchida, M.A., Amodaj, N., Pinkard, H., Vale, R.D., and Stuurman, N. (2014). Advanced methods of microscope control using μManager software. 2014.

Erbguth, K., Prigge, M., Schneider, F., Hegemann, P., and Gottschalk, A. (2012). Bimodal activation of different neuron classes with the spectrally red-shifted channelrhodopsin chimera C1V1 in Caenorhabditis elegans. PLoS ONE *7*, e46827.

Gao, S., Guan, S.A., Fouad, A.D., Meng, J., Kawano, T., Huang, Y.C., Li, Y., Alcaire, S., Hung, W., Lu, Y.*, et al.* (2018). Excitatory motor neurons are local oscillators for backward locomotion. eLife *7*, e29915.

Han, Y., Kaeser, P.S., Sudhof, T.C., and Schneggenburger, R. (2011). RIM determines Ca(2)+ channel density and vesicle docking at the presynaptic active zone. Neuron *69*, 304-316.

Held, R.G., Liu, C., Ma, K., Ramsey, A.M., Tarr, T.B., De Nola, G., Wang, S.H., Wang, J., van den Maagdenberg, A.M., Schneider, T.*, et al.* (2020). Synapse and Active Zone Assembly in the Absence of Presynaptic Ca2+ Channels and Ca2+ Entry. Neuron *107*, 1-17.

Hermann, A., Liewald, J.F., and Gottschalk, A. (2015). A photosensitive degron enables acute light-induced protein degradation in the nervous system. Current Biology *25*, R749-R750.

Hibino, H., Pironkova, R., Onwumere, O., Vologodskaia, M., Hudspeth, A.J., and Lesage, F. (2002). RIM binding proteins (RBPs) couple Rab3-interacting molecules (RIMs) to voltage-gated Ca(2+) channels. Neuron *34*, 411-423.

Hochbaum, D.R., Zhao, Y., Farhi, S.L., Klapoetke, N., Werley, C.A., Kapoor, V., Zou, P., Kralj, J.M., Maclaurin, D., Smedemark-Margulies, N.*, et al.* (2014). All-optical electrophysiology in mammalian neurons using engineered microbial rhodopsins. Nat Methods *11*, 825-833.

Huang, Y.C., Pirri, J.K., Rayes, D., Gao, S., Mulcahy, B., Grant, J., Saheki, Y., Francis, M.M., Zhen, M., and Alkema, M.J. (2019). Gain-of-function mutations in the UNC-2/CaV2alpha channel lead to excitation-dominant synaptic transmission in Caenorhabditis elegans. eLife *8*.

Kaeser, P.S., Deng, L., Wang, Y., Dulubova, I., Liu, X., Rizo, J., and Sudhof, T.C. (2011). RIM proteins tether Ca2+ channels to presynaptic active zones via a direct PDZ-domain interaction. Cell *144*, 282-295.

Kittelmann, M., Hegermann, J., Goncharov, A., Taru, H., Ellisman, M.H., Richmond, J.E., Jin, Y., and Eimer, S. (2013a). Liprin-alpha/SYD-2 determines the size of dense projections in presynaptic active zones in C. elegans. J Cell Biol *203*, 849-863.

Kittelmann, M., Liewald, J.F., Hegermann, J., Schultheis, C., Brauner, M., Steuer Costa, W., Wabnig, S., Eimer, S., and Gottschalk, A. (2013b). In vivo synaptic recovery following optogenetic hyperstimulation. Proc Natl Acad Sci U S A *110*, E3007-3016.

Koushika, S.P., Richmond, J.E., Hadwiger, G., Weimer, R.M., Jorgensen, E.M., and Nonet, M.L. (2001). A post-docking role for active zone protein Rim. Nat Neurosci *4*, 997-1005.

Kralj, J.M., Douglass, A.D., Hochbaum, D.R., Maclaurin, D., and Cohen, A.E. (2012). Optical recording of action potentials in mammalian neurons using a microbial rhodopsin. Nat Methods *9*, 90-95.

Kushibiki, Y., Suzuki, T., Jin, Y., and Taru, H. (2019). RIMB-1/RIM-Binding Protein and UNC-10/RIM Redundantly Regulate Presynaptic Localization of the Voltage-Gated Calcium Channel in Caenorhabditis elegans. J Neurosci *39*, 8617-8631.

Laine, V., Frokjaer-Jensen, C., Couchoux, H., and Jospin, M. (2011). The alpha1 subunit EGL-19, the alpha2/delta subunit UNC-36, and the beta subunit CCB-1 underlie voltage-dependent calcium currents in Caenorhabditis elegans striated muscle. J Biol Chem *286*, 36180-36187.

Liewald, J.F., Brauner, M., Stephens, G.J., Bouhours, M., Schultheis, C., Zhen, M., and Gottschalk, A. (2008). Optogenetic analysis of synaptic function. Nat Methods *5*, 895-902.

Liu, H., Li, L., Wang, W., Gong, J., Yang, X., and Hu, Z. (2018). Spontaneous Vesicle Fusion Is Differentially Regulated at Cholinergic and GABAergic Synapses. Cell reports *22*, 2334-2345.

Liu, K.S., Siebert, M., Mertel, S., Knoche, E., Wegener, S., Wichmann, C., Matkovic, T., Muhammad, K., Depner, H., Mettke, C.*, et al.* (2011). RIM-binding protein, a central part of the active zone, is essential for neurotransmitter release. Science *334*, 1565-1569.

Liu, P., Chen, B., Mailler, R., and Wang, Z.W. (2017). Antidromic-rectifying gap junctions amplify chemical transmission at functionally mixed electrical-chemical synapses. Nature communications *8*, 14818.

Liu, P., Chen, B., and Wang, Z.-W. (2020). GABAergic motor neurons bias locomotor decision-making in C. elegans. Nature communications *11*, 5076.

Liu, Q., Hollopeter, G., and Jorgensen, E.M. (2009). Graded synaptic transmission at the Caenorhabditis elegans neuromuscular junction. Proc Natl Acad Sci U S A *106*, 10823-10828.

Lubbert, M., Goral, R.O., Satterfield, R., Putzke, T., van den Maagdenberg, A.M., Kamasawa, N., and Young, S.M., Jr. (2017). A novel region in the CaV2.1 alpha1 subunit C-terminus regulates fast synaptic vesicle fusion and vesicle docking at the mammalian presynaptic active zone. eLife *6*.

Mahoney, T.R., Luo, S., and Nonet, M.L. (2006). Analysis of synaptic transmission in Caenorhabditis elegans using an aldicarb-sensitivity assay. Nat Protoc *1*, 1772-1777.

Maro, G.S., Gao, S., Olechwier, A.M., Hung, W.L., Liu, M., Ozkan, E., Zhen, M., and Shen, K. (2015). MADD-4/Punctin and Neurexin Organize C. elegans GABAergic Postsynapses through Neuroligin. Neuron *86*, 1420-1432.

Muller, M., Genc, O., and Davis, G.W. (2015). RIM-binding protein links synaptic homeostasis to the stabilization and replenishment of high release probability vesicles. Neuron *85*, 1056-1069.

Nanou, E., and Catterall, W.A. (2018). Calcium Channels, Synaptic Plasticity, and Neuropsychiatric Disease. Neuron *98*, 466-481.

Oranth, A., Schultheis, C., Tolstenkov, O., Erbguth, K., Nagpal, J., Hain, D., Brauner, M., Wabnig, S., Steuer Costa, W., McWhirter, R.D.*, et al.* (2018). Food Sensation Modulates Locomotion by Dopamine and Neuropeptide Signaling in a Distributed Neuronal Network. Neuron *100*, 1414-1428 e1410.

Schindelin, J., Arganda-Carreras, I., Frise, E., Kaynig, V., Longair, M., Pietzsch, T., Preibisch, S., Rueden, C., Saalfeld, S., Schmid, B.*, et al.* (2012). Fiji: an open-source platform for biological-image analysis. Nature Methods *9*, 676-682.

Schultheis, C., Brauner, M., Liewald, J.F., and Gottschalk, A. (2011). Optogenetic analysis of GABAB receptor signaling in Caenorhabditis elegans motor neurons. J Neurophysiol *106*, 817-827.

Steuer Costa, W., Yu, S.C., Liewald, J.F., and Gottschalk, A. (2017). Fast cAMP Modulation of Neurotransmission via Neuropeptide Signals and Vesicle Loading. Curr Biol *27*, 495-507.

Sudhof, T.C. (2012). Calcium control of neurotransmitter release. Cold Spring Harb Perspect Biol *4*, a011353.

Sudhof, T.C. (2013). Neurotransmitter release: the last millisecond in the life of a synaptic vesicle. Neuron *80*, 675-690.

Wang, Y., Sugita, S., and Sudhof, T.C. (2000). The RIM/NIM family of neuronal C2 domain proteins. Interactions with Rab3 and a new class of Src homology 3 domain proteins. J Biol Chem *275*, 20033-20044.

Watanabe, S., Liu, Q., Davis, M.W., Hollopeter, G., Thomas, N., Jorgensen, N.B., and Jorgensen, E.M. (2013). Ultrafast endocytosis at Caenorhabditis elegans neuromuscular junctions. eLife *2*, e00723.

Wu, X., Cai, Q., Shen, Z., Chen, X., Zeng, M., Du, S., and Zhang, M. (2019). RIM and RIM-BP Form Presynaptic Active-Zone-like Condensates via Phase Separation. Molecular Cell *73*, 971-984.e975.

Yu, S.C., Janosi, B., Liewald, J.F., Wabnig, S., and Gottschalk, A. (2018). Endophilin A and B Join Forces With Clathrin to Mediate Synaptic Vesicle Recycling in Caenorhabditis elegans. Frontiers in molecular neuroscience *11*, 196.

Figures and Figure Legends

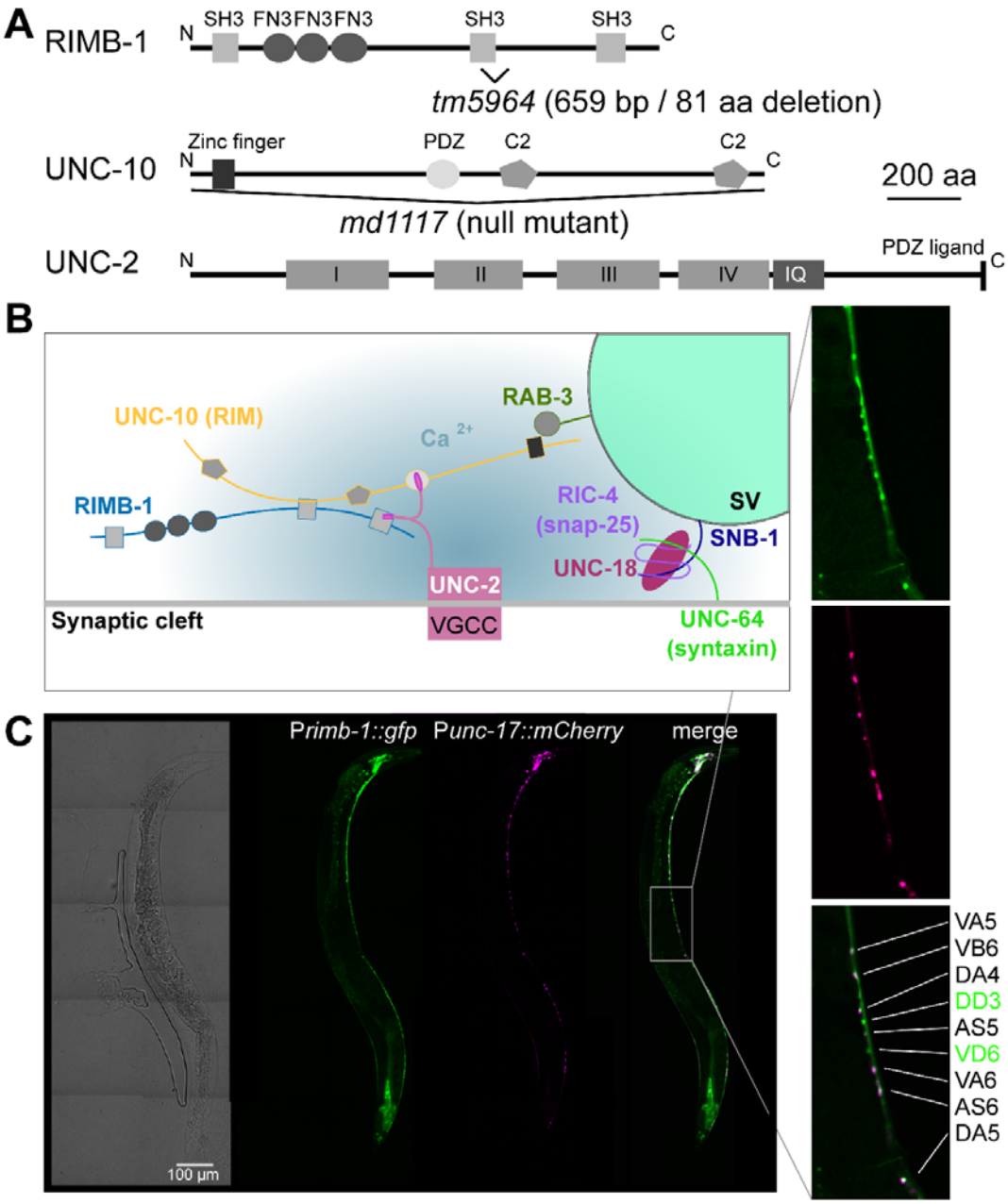

Figure 1: UNC-10/RIM and RIMB-1/RIM-binding protein affect UNC-2/Cav2 function in *C. elegans* (motor) neurons. A) Protein primary structures and sequence features (SH3 – src homology 3; FN3 – fibronectin 3; PDZ – PDZ domain; C2 – Ca^{2+} and phospholipid binding domain; I-IV – VGCC modules; IQ – IQ domain) of RIMB-1, UNC-10/RIM, and UNC-2/Ca_v2. Deletion sites of alleles used in this work are indicated. **B)** Arrangement of proteins anchoring the UNC-2 channel in the vicinity of a docked SV. **C)** Brightfield and fluorescence micrographs of an animal expressing GFP from the *rimb-1p* promoter and mCherry from the *unc-17p* promoter (cholinergic neurons). RIMB-1 appears to be pan-neuronal, and in the ventral nerve cord, is expressed in cholinergic (magenta and green) and GABAergic motor neurons (green only). Scale bar: 100 µm.

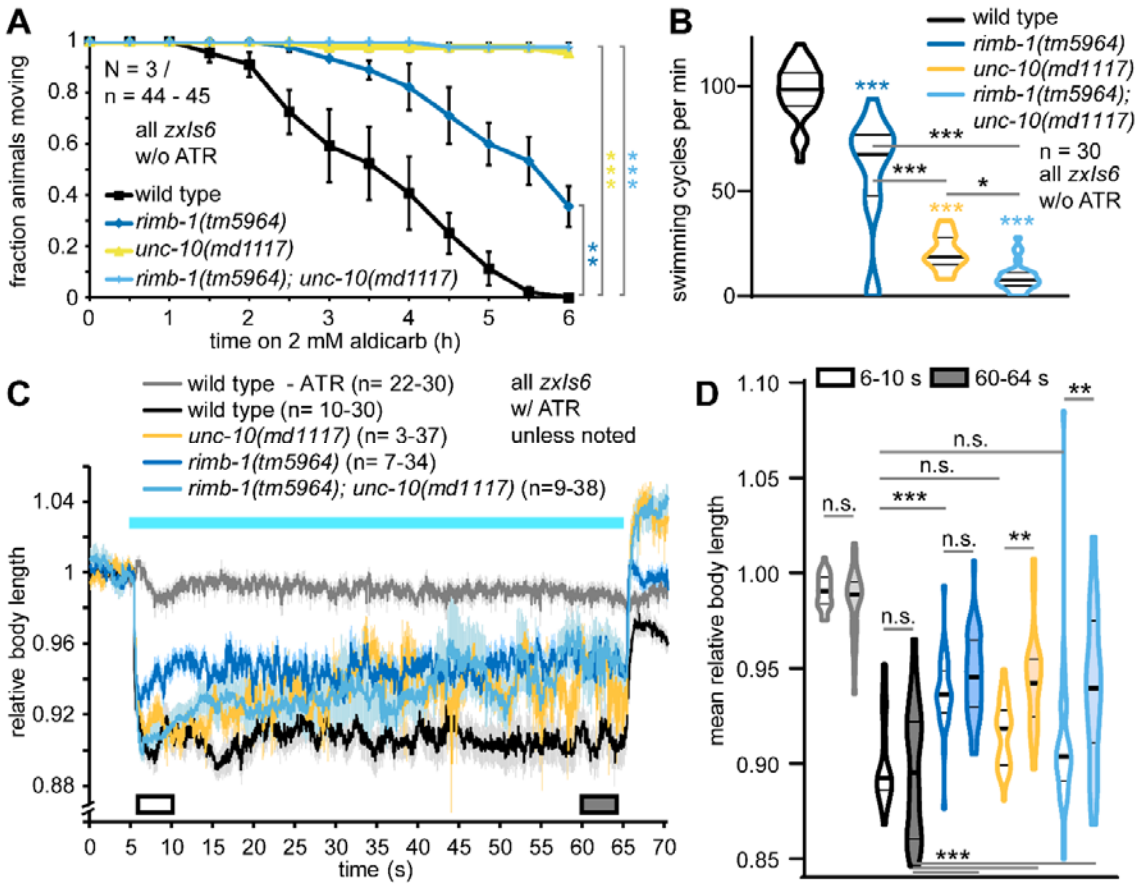

Figure 2: *rimb-1* mutants exhibit defective cholinergic transmission, locomotion and muscle activation. A) Aldicarb paralysis assay probing cholinergic transmission; progressive paralysis is delayed in mutants. The indicated genotypes and number of animals were scored and data from 3 experiments averaged at the indicated time points. Mean ± s.e.m. Log rank test, Bonferroni correction. **B)** Swimming locomotion assay of the indicated genotypes (n=30 animals each). Animals were left swimming in liquid and their full body thrashes during 1 min were counted. Data shown as median and 25/75 quartiles (thick and thin lines), min to max. Statistical significance determined by one-way ANOVA, Bonferroni-corrected. **C)** Photostimulated cholinergic transmission causes muscle contraction, measured by video microscopy. Relative body length of the indicated number of animals (mean ± s.e.m.) of the indicated genotypes, before, during and after a 1 min photostimulus (blue bar). +/-ATR: presence/absence of all-*trans* retinal, rendering ChR2 functional (or not). White and grey boxes indicate periods for which statistical comparisons were calculated in **D)** Data in C) (6-10 and 60-64 s) shown as median and 25/75 quartiles (thick and thin lines), min to max. One-way ANOVA, Tukey test. In A, B, D: Statistical significance given as *p<0.05; **p<0.01; ***p<0.001.

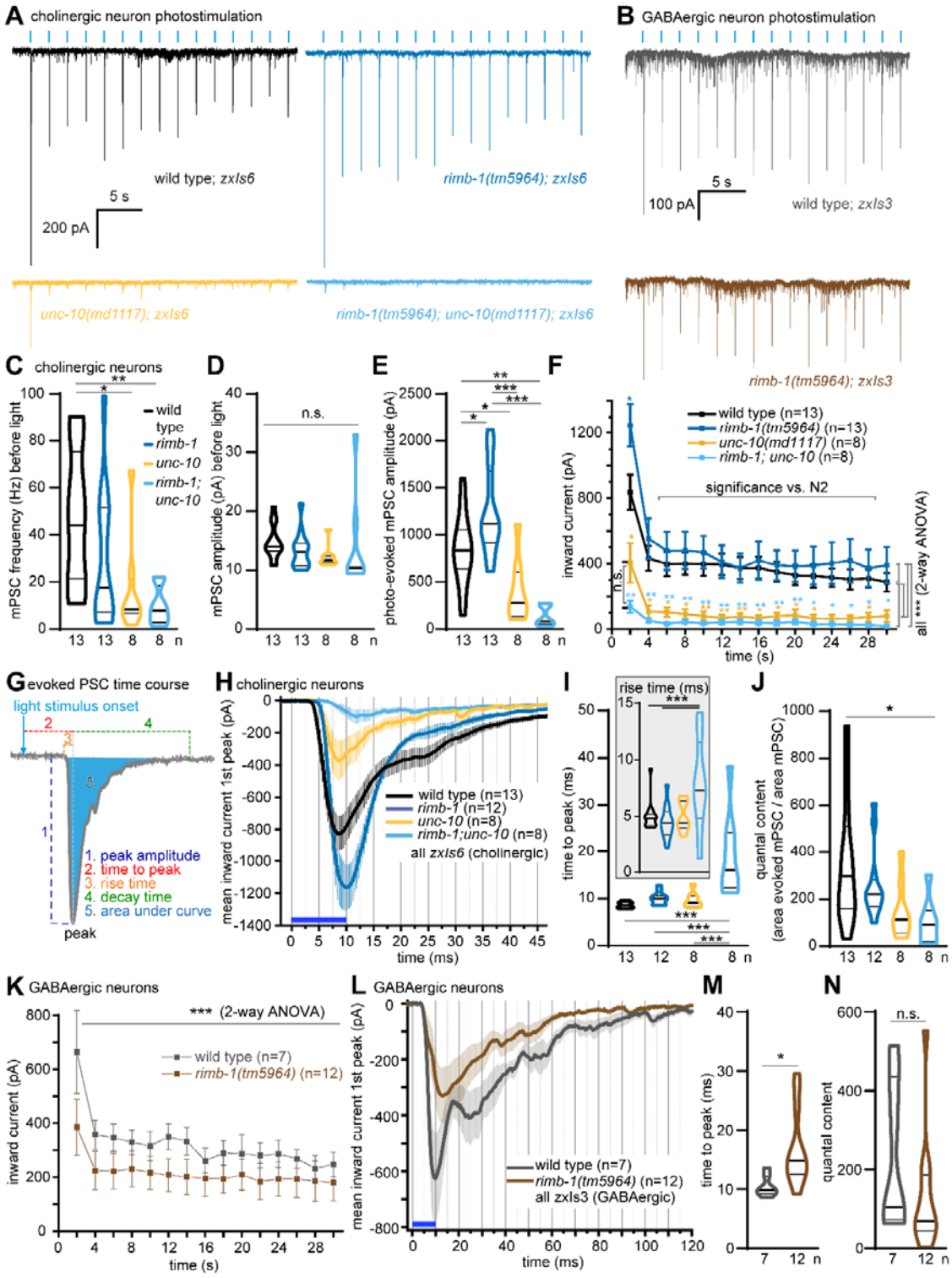

Figure 3: Electrophysiological phenotypes at the neuromuscular junction of *rimb-1* mutants. A) Photo-stimulation of cholinergic motor neurons induces post-synaptic currents. Shown are original records for the indicated genotypes, induced by 0.5 Hz, 10 ms stimuli (blue tick marks) of animals bearing transgene *zxIs6* (ChR2 in cholinergic neurons, expressed from promoter *unc-17p*). **B)** As in A, animals carry transgene *zxIs3*, expressing ChR2 in GABAergic neurons (promoter *unc-47p*). Miniature post-synaptic current (mPSC)

frequencies **C)** and amplitudes **D)** during 30 s before first light stimulus. Data shown as median and 25/75 quartiles (thick and thin lines), min to max. One-way ANOVA, Kruskall-Wallis test. **E)** Photoevoked (*zxIs6*) post-synaptic current (ePSC) amplitude of the first, and consecutive **F)** photostimuli (mean ± s.e.m.). One-way ANOVA with Tukey test in E, and for individual stimuli in F; two-way ANOVA in F to compare entire datasets. **G)** Analysis of ePSC properties, relative to the onset of the light stimulus (blue arrow). 1: peak amplitude; 2: time from light onset to peak; 3: rise time (from current onset to peak); 4: decay time (from peak to baseline); 5: area under the curve (charge transfer). **H)** High-resolution analysis of first light-evoked cholinergic peak current, mean ± s.e.m. **I)** Group data analysis of time to peak and rise time (inset). **J)** Quantal content, calculated as the area under the curve (ePSC) divided by the mPSC area under curve, from data in A. One-way ANOVA and Tukey test in I and Newman-Keuls test in J. **K-M)** As in F, H, I, J, but for GABAergic stimulation (*zxIs3*). In C-F, I-K, M: Statistical significance given as *p<0.05; **p<0.01; ***p<0.001.

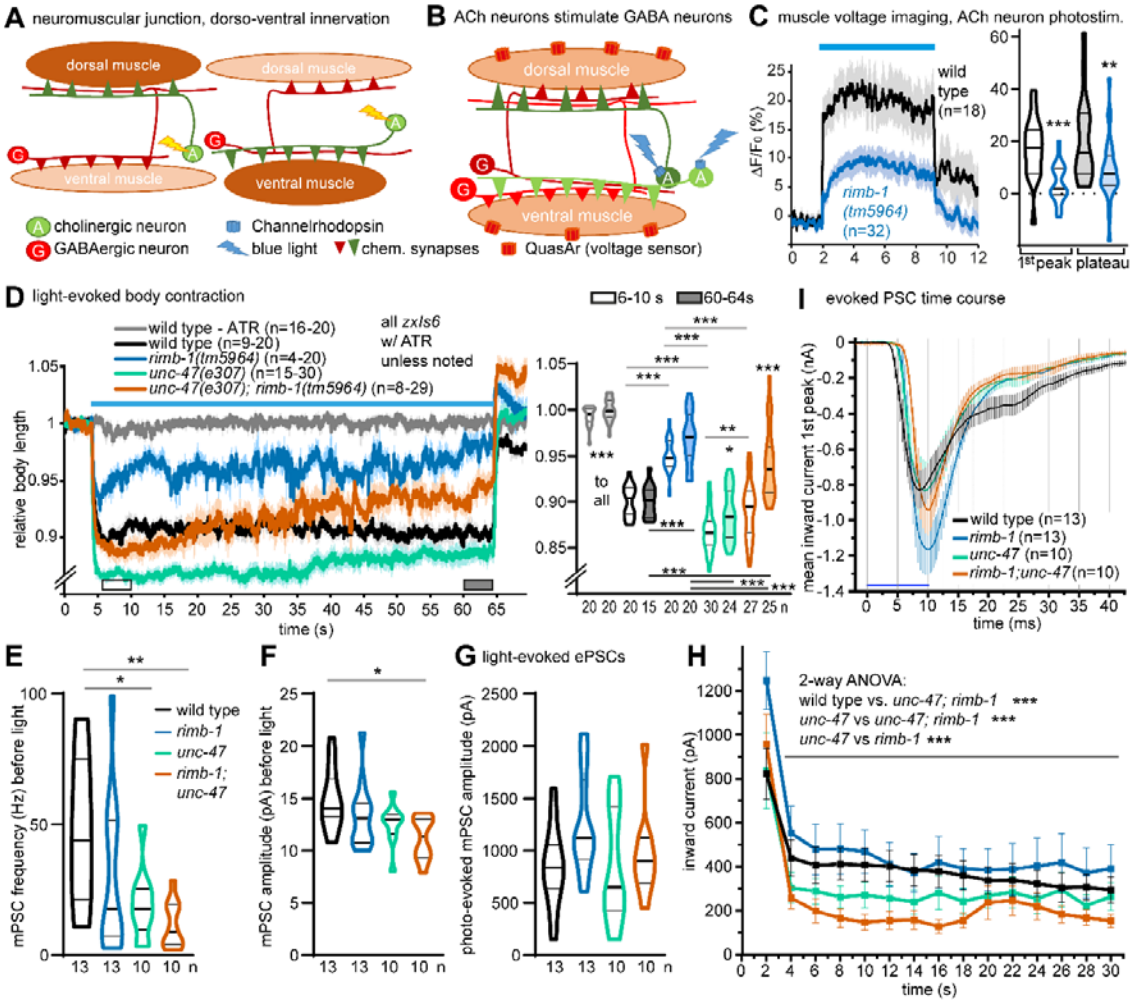

Figure 4: RIMB-1 acts differently in cholinergic and GABAergic motor neurons, affecting overall NMJ transmission. A) Organization of the *C. elegans* NMJ: Reciprocal innervation of muscle by cholinergic (A, green) and GABAergic (G, red) neurons, and further contralateral innervation of GABAergic neurons by cholinergic neurons. Dorsal or ventral stimulation (flashes) causes antagonistic inhibition, enabling undulatory locomotion. **B)**

Optogenetic stimulation of cholinergic neurons (blue flashes) causes concomitant GABAergic release. **C)** Voltage imaging of muscle depolarization following cholinergic photostimulation. Muscles express the Arch(D95N) voltage sensor, fluorescence increases during photostimulation (blue bar); compared to *rimb-1* animals. Group data (peak response, plateau) shown as median and 25/75 quartiles (thick and thin lines), min to max. One-way ANOVA, Tukey test. **D)** Left panel: Body contraction after photostimulation of cholinergic neurons (*zxIs6*). Indicated genotypes and number of animals. Right panel: Group data for the 6-10 / 60-64 s time periods. Significant differences after one-way ANOVA with Tukey test (for same period) and two-way ANOVA with Bonferroni correction (for different time periods). **E)** mPSC frequencies and **F)** amplitudes during 30 s before first light stimulus for the indicated strains expressing ChR2 in cholinergic neurons (*zxIs6*). Data shown as median and 25/75 quartiles (thick and thin lines), min to max. n = number of animals. One-way ANOVA, Tukey test. **G)** Photoevoked PSC amplitude of first and **H)** consecutive photostimuli (mean ± s.e.m.). Two-way ANOVA with Fisher test in H to compare datasets. **I)** Time-course of ePSCs (first peak; blue bar: light stimulus); mean ± s.e.m. In C, D, E-H: Statistical significance given as *p<0.05; **p<0.01; ***p<0.001.

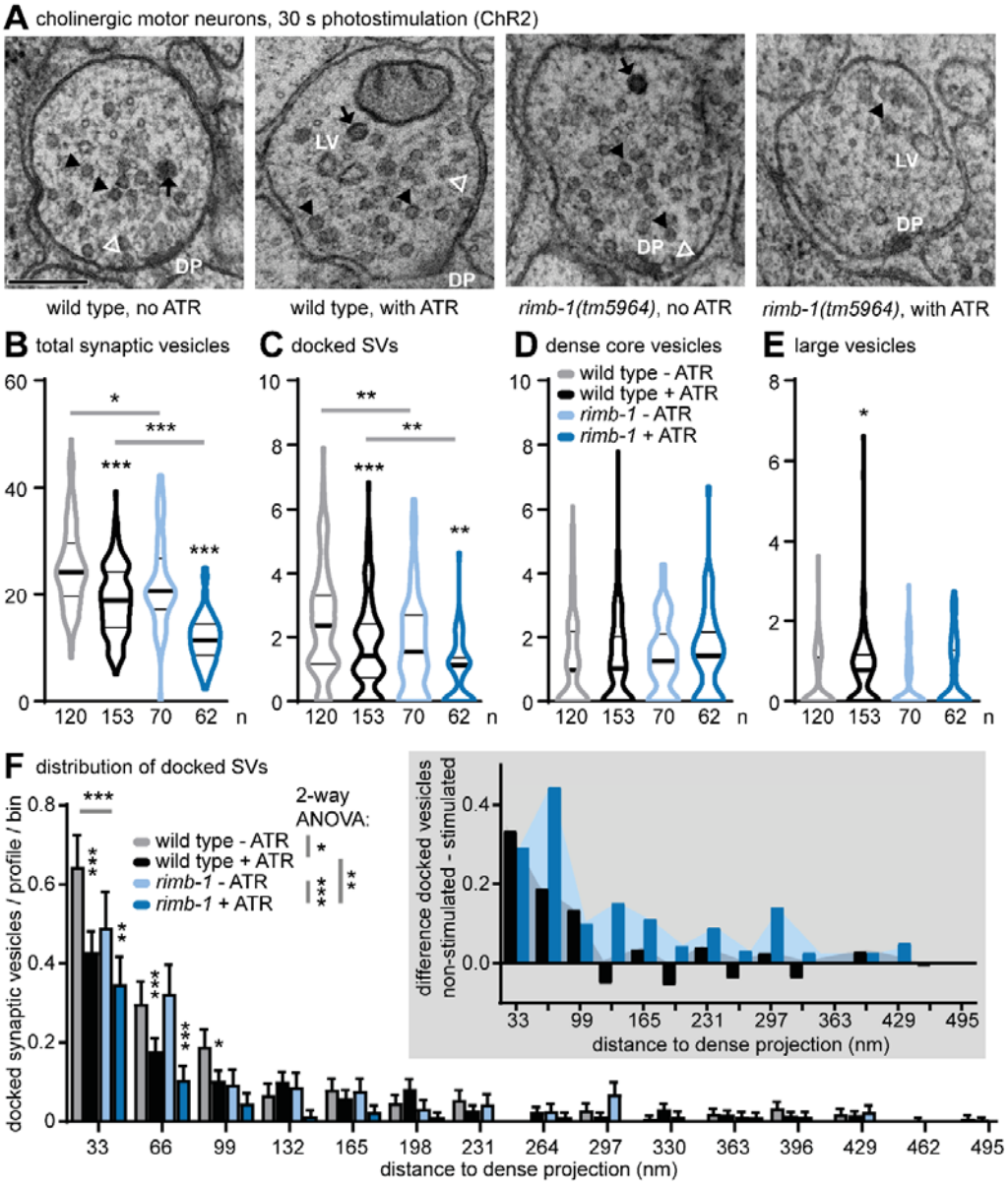

Figure 5: Electron microscopy analysis of photostimulated cholinergic *rimb-1* synapses. A) Transmission electron micrographs of cholinergic synapses expressing ChR2 (*zxIs6*), from animals that were high-pressure frozen following 30 s of photostimulation. 40 nm sections; genotype and ATR treatment indicated. Synaptic vesicles (SVs, closed arrowheads), docked SVs (open white arrowheads), dense core vesicles (DCVs, black arrows), large vesicles (LV, i.e. endosomes induced after photostimulation), and the dense projections (DP) are indicated. Scale bar is 200 nm. **B)** Quantification of all SVs, **C)** docked SVs, **D)** DCVs, and **E)** LVs, per profile. Data in B-E shown as median and 25/75 quartiles (thick and thin lines), min to max. One-way ANOVA with Kruskall-Wallis / Dunn's multiple comparison test. **F)** The distribution of distances of docked SVs to the DP (along the plasma membrane) was analyzed in 33 nm bins, for the genotypes indicated. Two-way ANOVA / Tukey test (within bins, between groups). Inset: Difference in the number of docked SVs (normalized to 33 nm bin, no ATR) in each bin without photostimulation, minus with photostimulation (i.e. showing where SVs disappeared). See also **Fig. S7B**. In B-F: Statistical significance given as *p<0.05; **p<0.01; ***p<0.001.

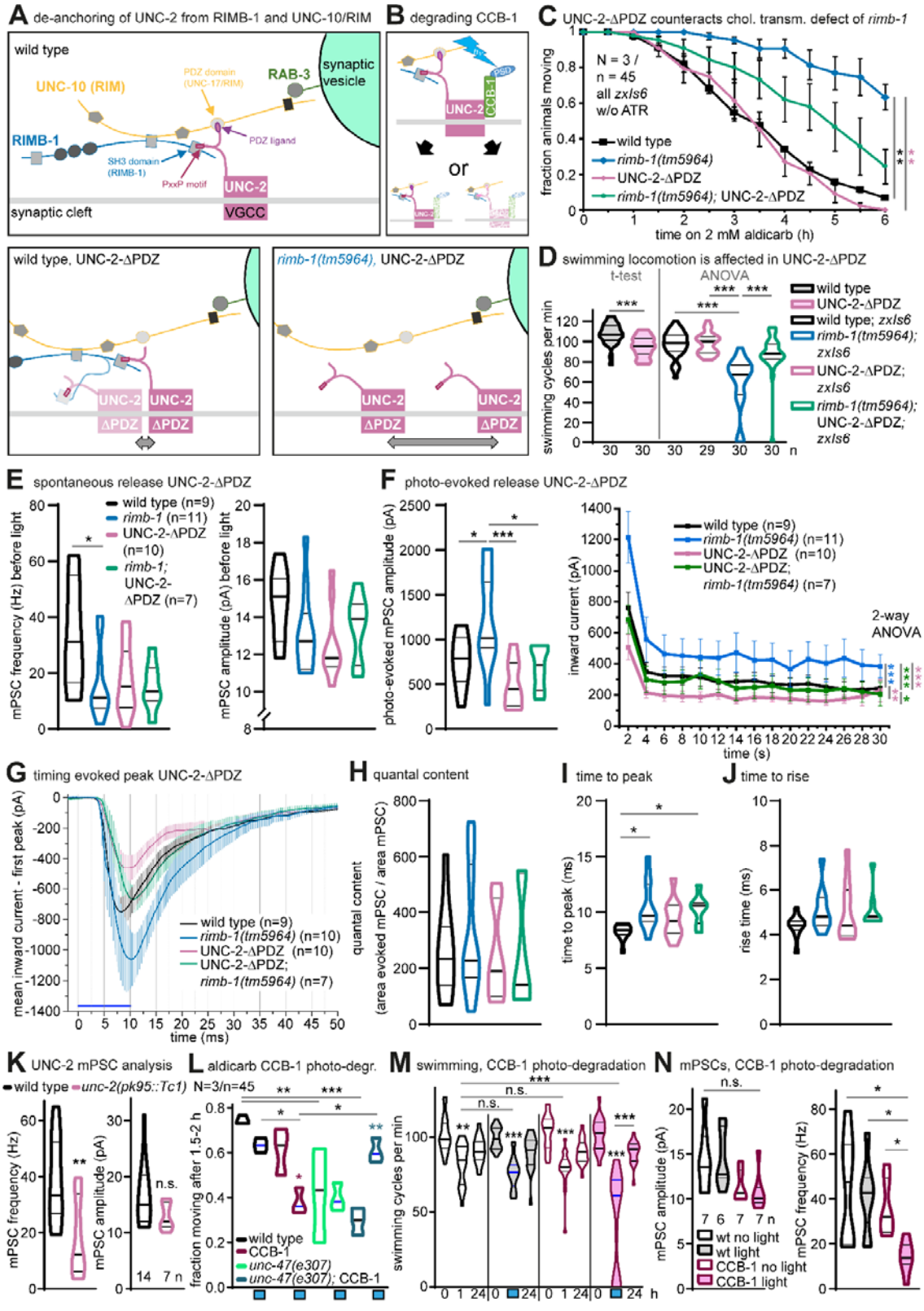

Figure 6: Untethering the Ca_v2 VGCC alters synaptic transmission, exacerbated by *rimb-1* deletion. A) Upper panel: Protein-protein interactions involving the Cav2(UNC-2) VGCC and RIMB-1. UNC-2 is tethered by interactions with RIMB-1 (PxxP motif bound by RIMB-1 SH3 domain) and RIM/UNC-10 (C-terminal PDZ ligand bound by UNC-10 PDZ

domain). Lower left panel: Removing the PDZ ligand might loosen UNC-2 tethering at the docked SV site. Lower right panel: Removing RIMB-1 further untethers the UNC-2 VGCC. **B)** Acutely inactivating (or destabilizing) UNC-2 by photodegradation of the β-subunit, CCB-1, tagged with a C-terminal photo-sensitive degron (PSD). **C)** Aldicarb paralysis assay, mean ± s.e.m., 3 replicates, n=15 animals each, genotypes indicated. Log rank test, Bonferroni correction. **D)** Swimming assay, comparing locomotion rate in the indicated mutants, compared to wild type. Data shown as median and 25/75 quartiles (thick and thin lines), min to max. T-test or one-way ANOVA with Tukey test. n = number of animals tested. **E)** Electrophysiological analysis of UNC-2-ΔPDZ animals, compared to controls. mPSC frequency and amplitudes, before photostimulation. One-way ANOVA, Tukey test. **F)** Photoevoked (cholinergic neurons, transgene *zxIs6*) PSC amplitudes of first and consecutive stimuli. One-way ANOVA, Newman-Keuls test and two-way ANOVA, Fisher test. n = number of animals tested. **G)** Time-course of first ePSC (mean ± s.e.m.) and analysis of ePSC parameters **H-I)** quantal content, time to peak and time to rise. One-way ANOVA, Kruskall-Wallis test. **K)** Analysis of mPSC frequency and amplitudes in *unc-2* l.o.f. mutant; T-test. **L)** Animals lacking the VGCC β-subunit CCB-1 after photodegradation were analyzed in aldicarb (1 mM) paralysis assay. Data averaged from the 1.5-2 h time points. Compared to wild type and to *unc-47* vGAT mutants, animals without or with photostimulation for 1h (blue bars). Two-way ANOVA with Tukey test. **M)** Swimming assay in CCB-1::PSD animals before and after photodegradation (blue bar, shaded data sets) and following 24 h recovery. Compared to wild type controls, and non-illuminated animals (non-shaded data sets). One way ANOVA with Bonferroni test within data sets (light and no light) and two-way ANOVA to compare datasets without and with illumination. **N)** mPSC analysis, frequency and amplitude, without and with CCB-1::PSD photo-degradation (1h), and wild type controls. One-way ANOVA, Newman-Keuls test. n = number of animals. In C-F, I-N: Statistical significance given as *p<0.05; **p<0.01; ***p<0.001.

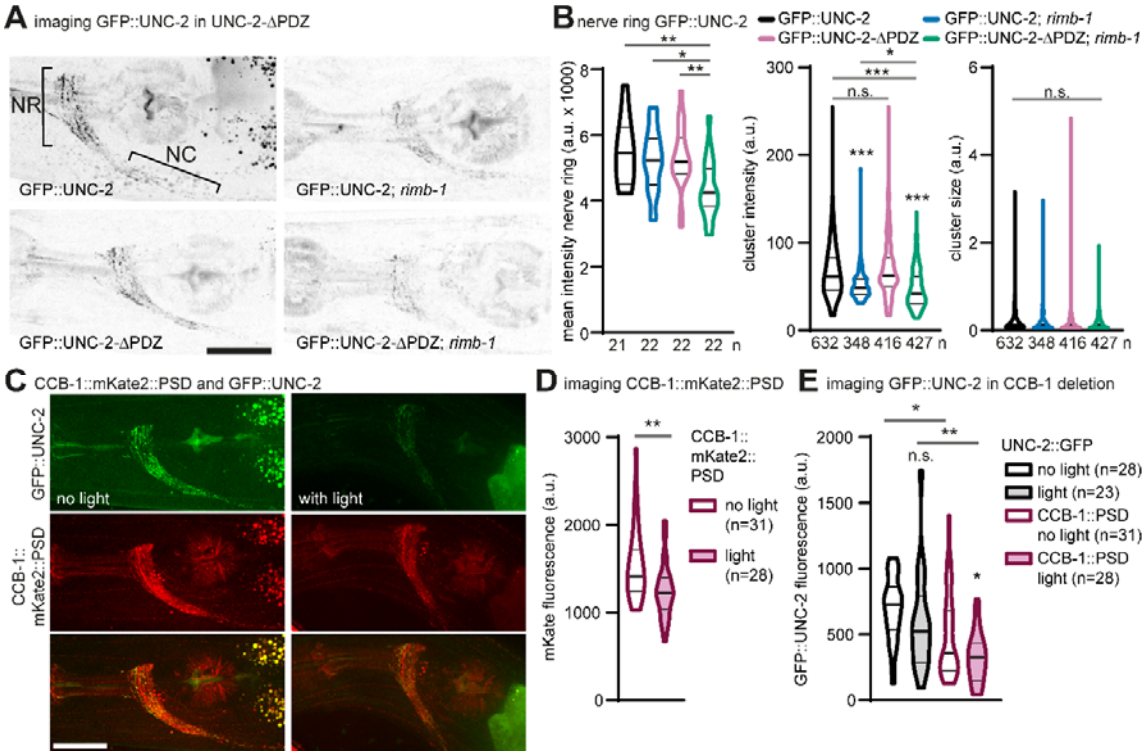

Figure 7: Cav2/UNC-2 channels are reduced at synapses in *rimb-1* mutants and after acute photodegradation of the CCB-1 β-subunit. A) Confocal z-projections of fluorescence of GFP::UNC-2 in the nerve ring (NR) and anterior ventral nerve cord (NC). Anterior is to the left, scale bar = 20 µm, genotypes as indicated. **B)** Quantification of fluorescent puncta (synaptic UNC-2 clusters) as shown in A, mean intensity of nerve ring (n= number of animals), mean cluster fluorescence and size (n= number of puncta). Data shown as median and 25/75 quartiles (thick and thin lines), min to max. One-way ANOVA with Tukey test or Kruskal-Wallis / Dunn's test. **C)** Confocal stacks of nerve ring fluorescence of GFP::UNC-2 (green) and CCB-1::mKate2::PSD (red), and overlay, before and after blue light activation of the PSD for 1 h; scale bar = 20 µm. **D)** CCB-1::mKate2::PSD fluorescence in the nerve ring, before and after blue light stimulation; n = number of animals analyzed. **E)** Quantification of GFP::UNC-2 in controls and in animals expressing CCB-1::mKate2::PSD, before and after 1 h blue illumination. Data shown as median and 25/75 quartiles (thick and thin lines), min to max. T-test or one-way ANOVA with Newman-Keuls test. In B, D: Statistical significance given as *p<0.05; **p<0.01; ***p<0.001.

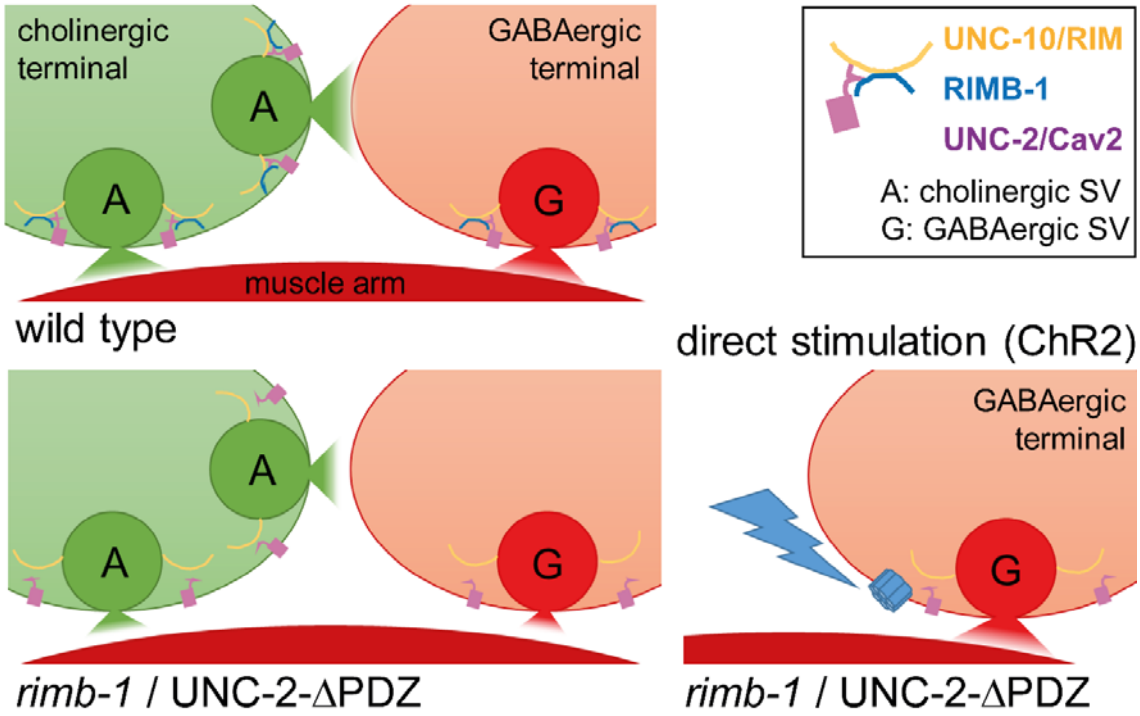

Figure 8: Model reconciling differential and summed effects of Cav2/UNC-2 untethering in *rimb-1* and ΔPDZ mutants at the NMJ of *C. elegans* (cholinergic and GABAergic synapses). Cholinergic stimulation co-activates GABAergic neurons. In *rimb-1*/UNC-2-ΔPDZ mutants, UNC-2 channels are mislocalized and transmission is reduced. These reducing effects are integrated in GABAergic neurons. When GABAergic neurons are directly stimulated using ChR2, these defects are less prominent.

Supplemental Figures and Legends

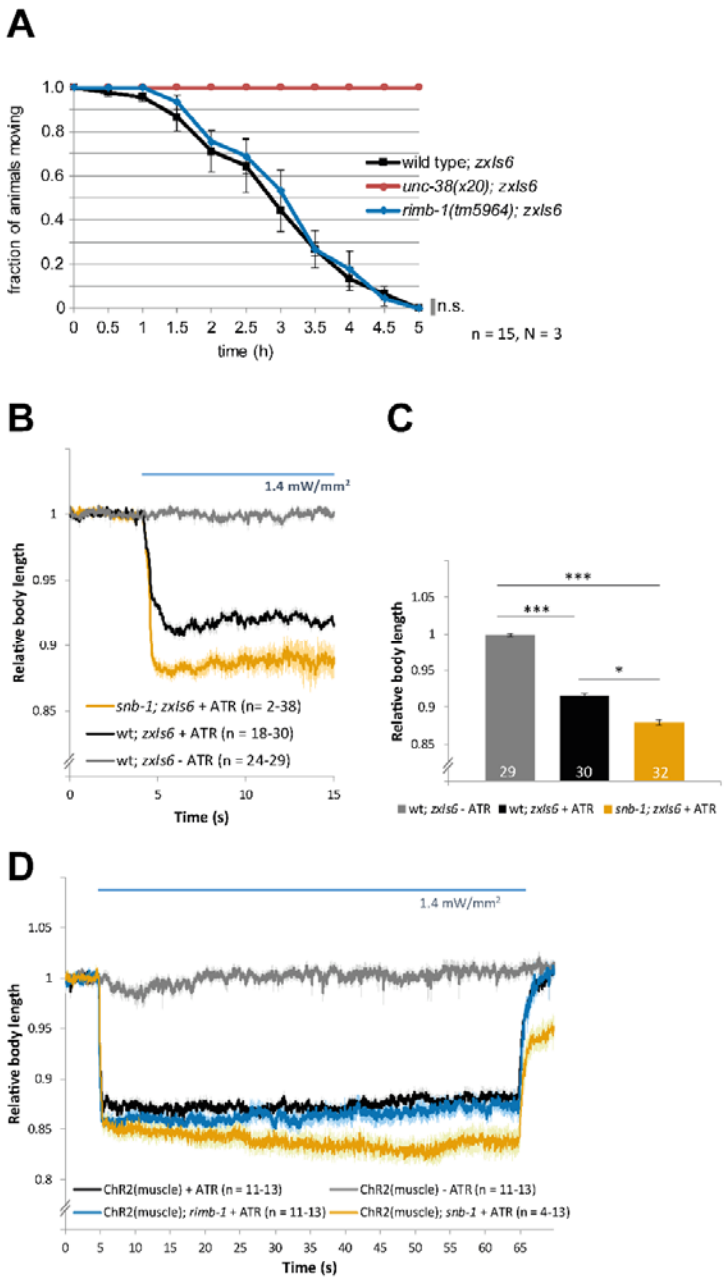

Figure S1: *rimb-1* mutants have no post-synaptic defect in muscular nAChRs, and normal muscle excitability. A) Levamisole-induced paralysis (1 mM, targeting muscular nAChRs), assessed over time, in three replicates, for the indicated number of animals of the indicated genotypes. Mean ± s.e.m. Log rank test. **B)** ChR2 expressed in cholinergic neurons, photoinduced muscle contraction (photostimulus indicated by blue bar). Shown is the mean (± s.e.m.) relative body length, n = number of animals. Synaptobrevin *snb-1(md247)* mutants show increased muscle contraction, despite reduced ACh release, due to compensatory excitability increase in post-synaptic muscle (Liewald et al., 2008). **C)** Statistical analysis of the data shown in B, one-way ANOVA, Bonferroni-corrected. **D)** Body

contraction induced by ChR2 expressed in muscle, demonstrating increased contractions in *snb-1* mutants, but normal excitability in *rimb-1* mutants. Statistical significance given as ***p<0.001.

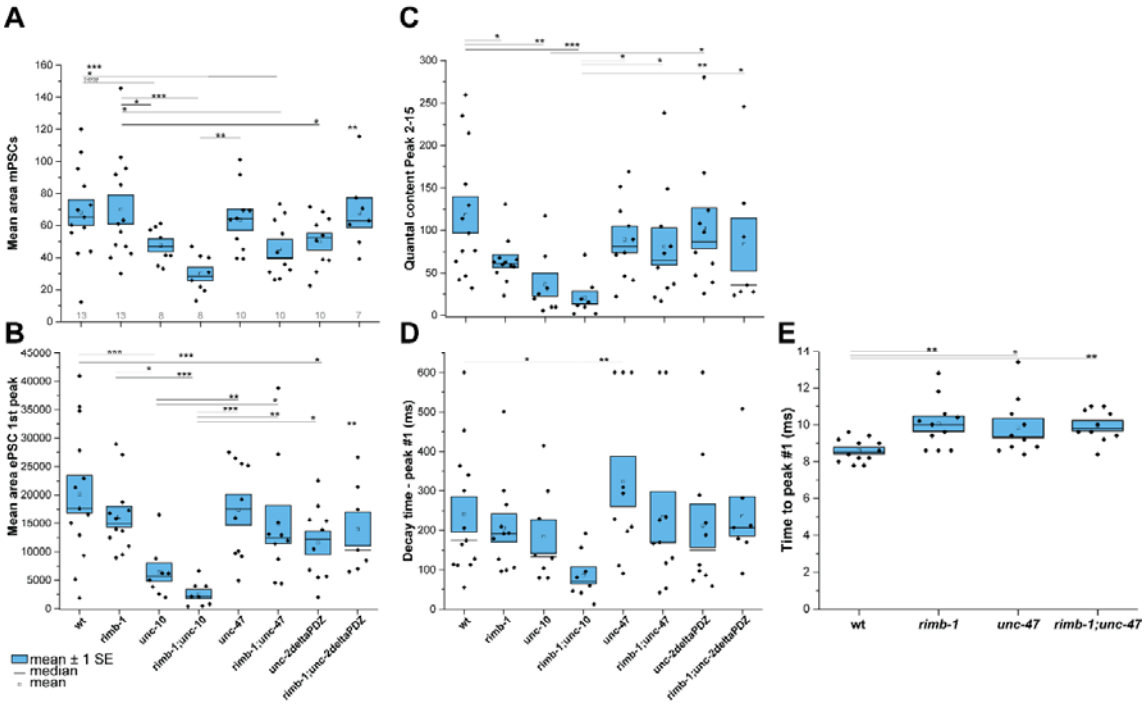

Figure S2: Parameters of mPSC and ePSC measurements acquired in this work; related to Figs. 3 and 4. A, B) Mean area of the mPSCs and first ePSCs for genotypes as indicated in B. Number of animals indicated in A. **C)** Quantal content as calculated from data in A and B. **D)** Decay time of the first photoevoked peak (*zxIs6*). **E)** Time to peak of the first photoevoked peak (*zxIs6*). Statistical significance after one-way ANOVA with Fisher test. Statistical significance given as *p<0.05; **p<0.01; ***p<0.001.

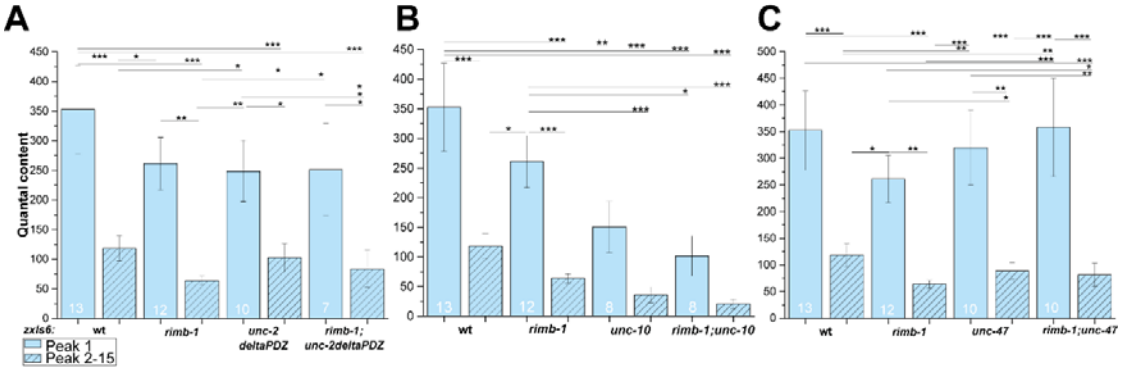

Figure S3: Quantal content of ePSC measurements acquired in this work; related to Figs. 3, 4 and 6. A-C) Quantal content calculated for first peak, and the average quantal content for the consecutive peaks 2-15, determined for the indicated genotypes after cholinergic photostimulation. Mean ± s.e.m. Statistical significance after one-way ANOVA

with Fisher test, given as *p<0.05; **p<0.01; ***p<0.001. Number of animals indicated in each bar.

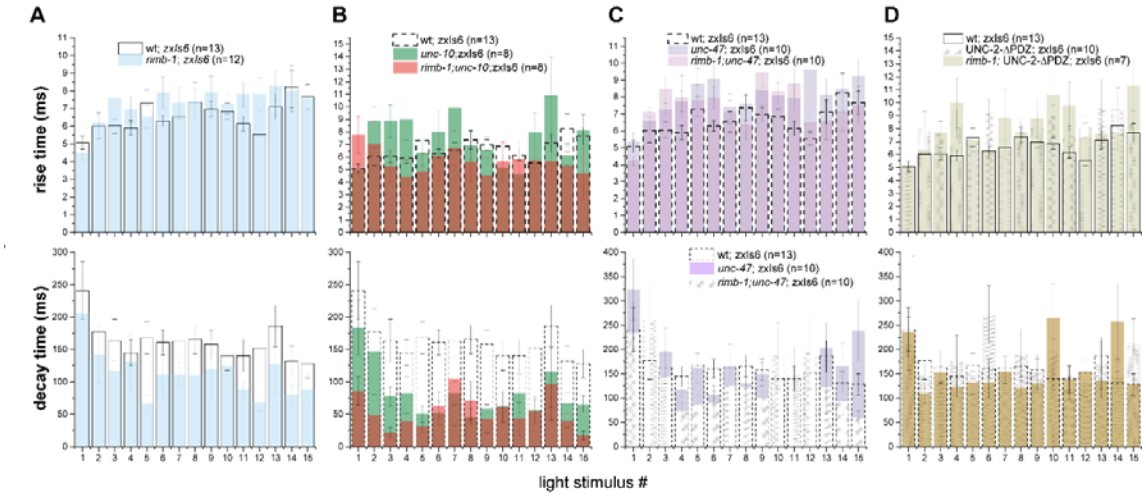

Figure S4: Rise and decay times of the 15 consecutive ePSC measurements acquired for different genotypes; related to Figs. 3, 4 and 6. A - D) Rise and decay times compared in wild type and the indicated mutant animals. Mean ± s.e.m. n, number of animals.

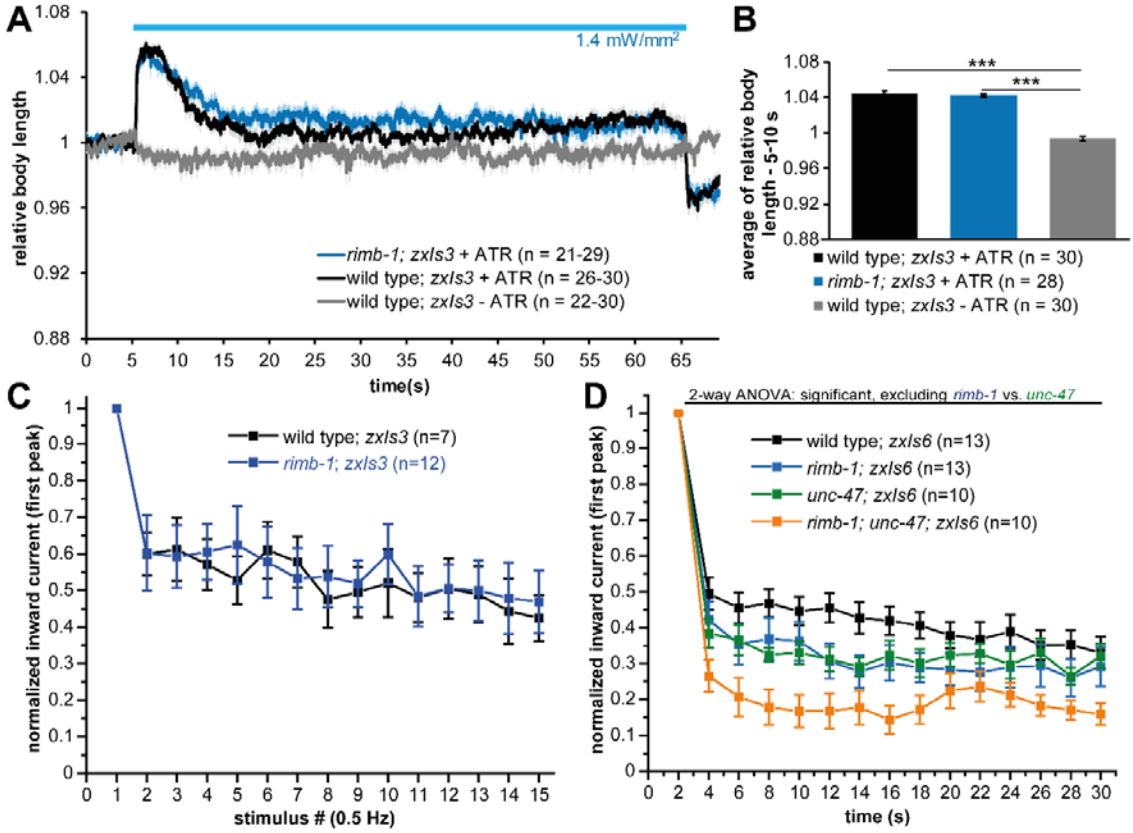

Figure S5: Optogenetically evoked GABAergic transmission at the NMJ is not largely affected in *rimb-1* mutants. A) Photostimulation of GABAergic neurons (transgene *zxIs3*)

causes body elongation. Genotypes and number of animals tested are indicated. **B)** Group data of the experiments shown in A, for the time period 1-5 s of the photostimulus; one-way ANOVA with Bonferroni correction. Statistical significance given as ***p<0.001. **C)** Photoevoked IPSCs for 15 consecutive stimuli, normalized to the first peak; means ± s.e.m. Related to **Fig. 3K**. No progressive change in the amplitude is apparent. **D)** Indirectly probing the GABAergic NMJ using cholinergic stimulation of GABAergic neurons, comparing wild type, *rimb-1* and *unc-47* vGAT mutants, normalized to the first peak. Related to **Fig. 4H**. 2-way ANOVA with Fisher test.

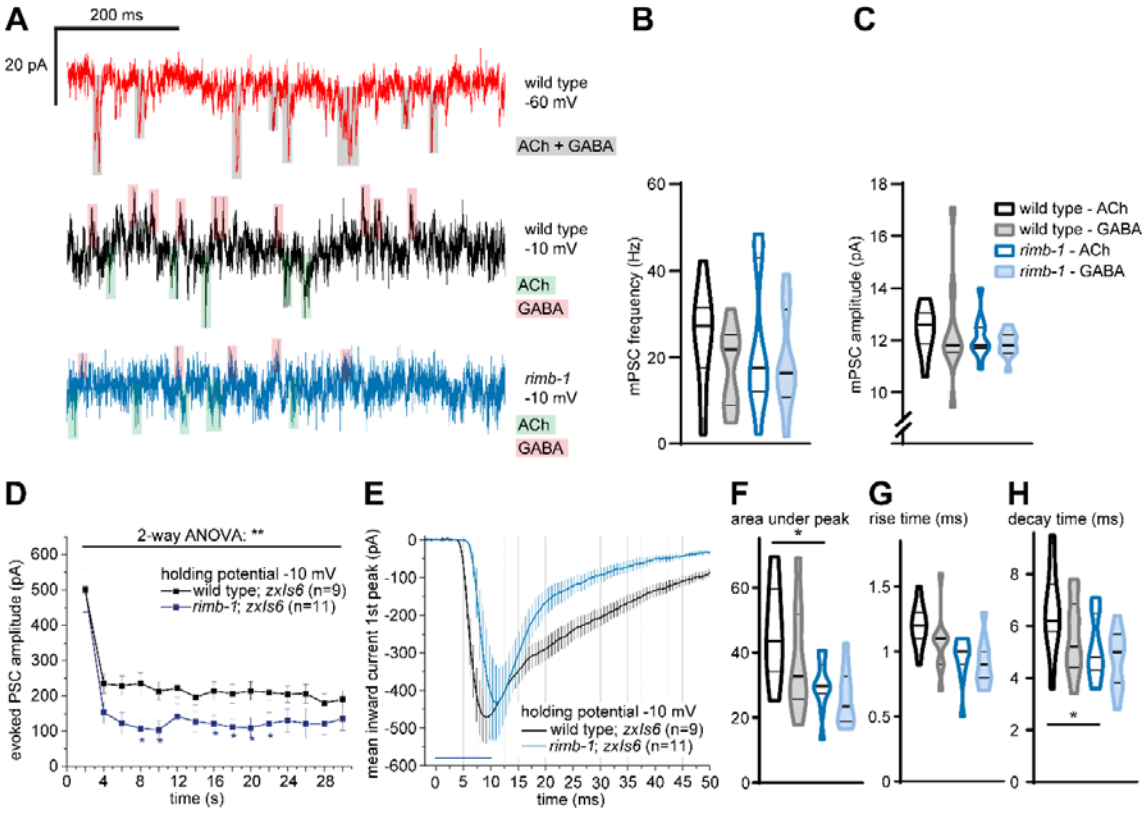

Figure S6: *rimb-1* defects in evoked NMJ transmission at -10 mV. A) mPSCs measured at different holding potentials (-60 mV or -10 mV), discerning cholinergic (green shade) and GABAergic (red shade) currents. Genotypes as noted. **B)** Frequency and **C)** amplitude, of cholinergic and GABAergic mPSCs, in wild type and *rimb-1(tm5964)* mutants. **D)** Mean (± s.e.m.) ePSCs for 15 consecutive cholinergic photo stimuli, measured at -10 mV. n = number of animals. **E)** Time course of first ePSC (mean ± s.e.m.), measured at -10 mV. Analysis of mPSC parameters **F)** area under peak, **G)** rise and **H)** decay time. One-way ANOVA with Tukey test. Data in B, C, F-H shown as median and 25/75 quartiles (thick and thin lines), min to max. Statistical significance in D, F given as *p<0.05; **p<0.01.

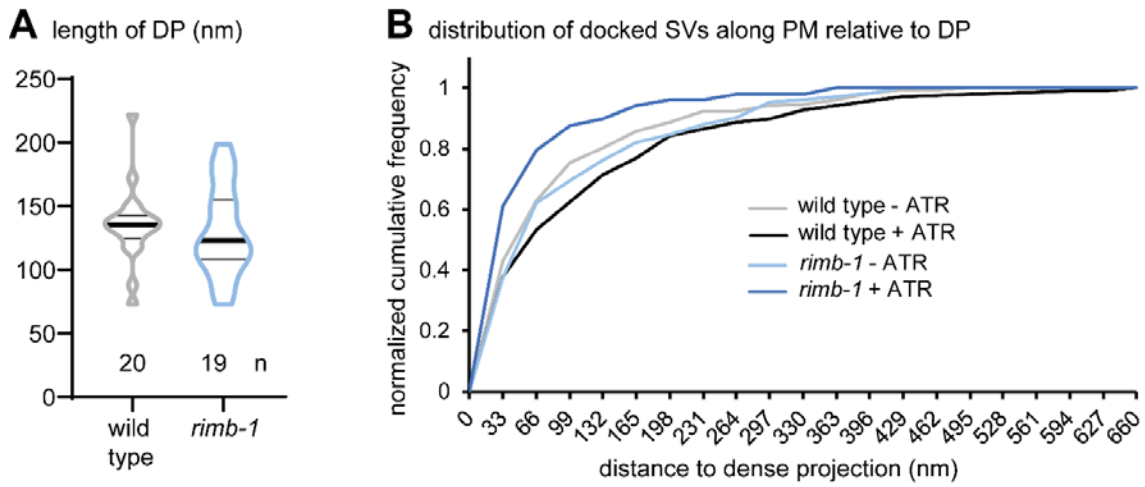

Figure S7: Ultrastructural parameters of *rimb-1* mutant synapses. A) Length of the dense projection was not altered in *rimb-1* synapses. **B)** Cumulative distribution of docked SVs in illuminated wild type vs. *rimb-1* mutant synapses, with or without ATR. Docked SVs in silent synapses are not differently distributed in *rimb-1* mutants, but fuse more distal to the DP. Related to **Fig. 5F**.

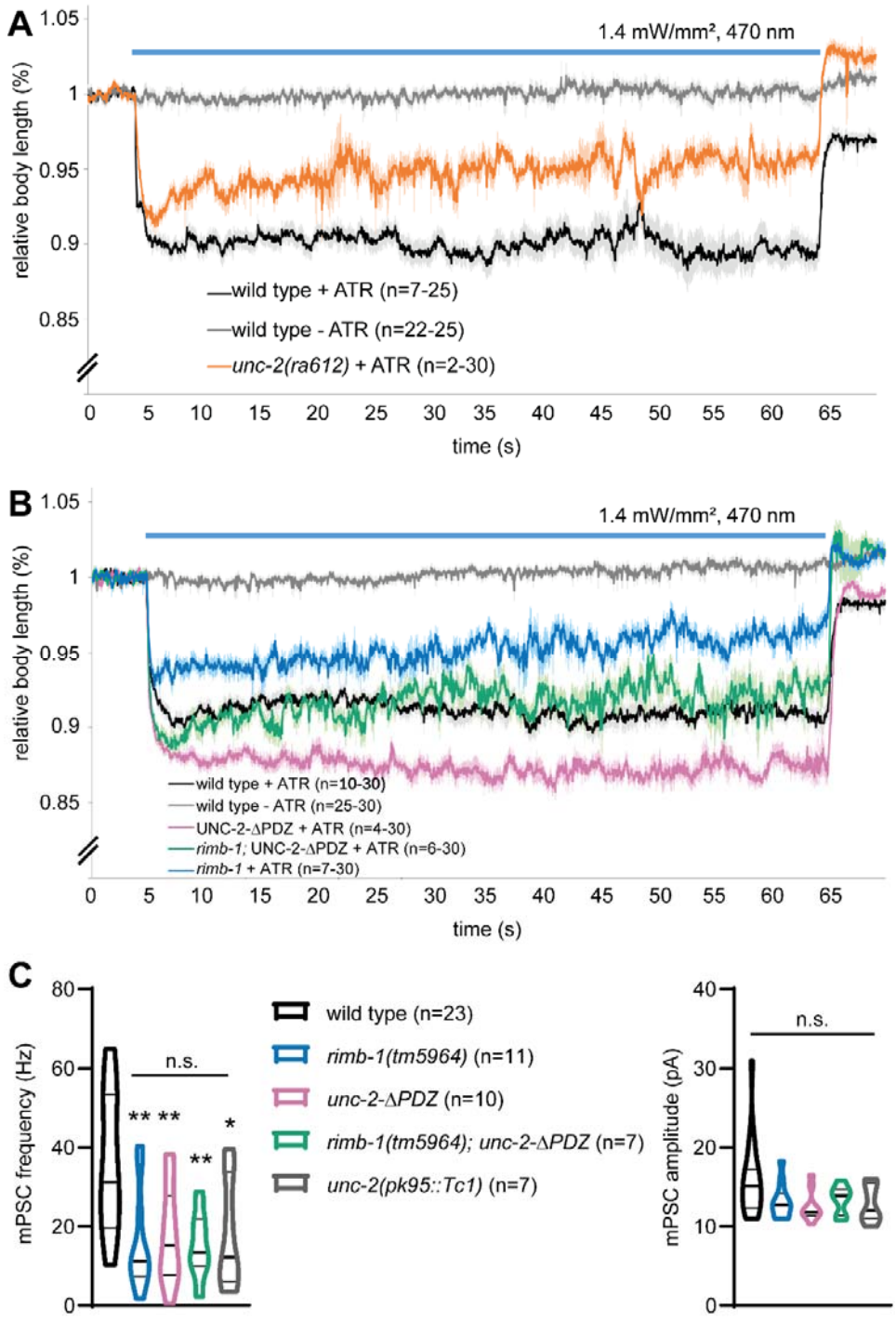

Figure S8: Differential effects of untethering and deleting Cav2/UNC-2 VGCCs on induced behavior and basal synaptic transmission. A, B) Photoinduced body contraction (transgene *zxIs6*) in *unc-2* deletion mutants, as well as *rimb-1*, UNC-2-ΔPDZ and *rimb-1*; UNC-2-ΔPDZ double mutants, compared to wild type controls. Mean ± s.e.m., light stimulus indicated by blue bar; n= number of animals analyzed. **C)** Spontaneous synaptic transmission, mPSC frequency and amplitude, compared in the indicated genotypes. n = number of animals, data shown as median and 25/75 quartiles (thick and thin lines), min to max. One-way ANOVA with Tukey test, *p<0.05, **p<0.01.